Perchlorate based 'over-saturated gel electrolyte' for an aqueous rechargeable hybrid Zn-Li battery

Shigang Chen,[†] *Rong Lan,*[†] *John Humphreys,*[†] *and Shanwen Tao**[†,‡]

[†]School of Engineering, University of Warwick, Coventry CV4 7AL, UK.

[‡]Department of Chemical Engineering, Monash University, Clayton, Victoria 3800.

Keywords over-saturated gel electrolyte, wide electrochemical window, quasi-solid-state, aqueous hybrid battery, zinc metal anode

Abstract: In this work, for the first time, 'over-saturated gel electrolyte' (OSGE) with extended electrochemical windows for electrolytes for use in aqueous batteries have been investigated. The stability window of 10 m $LiClO_4$-PVA OSGE is 3.3 V when saturated at 95 °C, which is 0.6 V wider than that of 2.7 V for the 6 m (saturated at room temperature) $LiClO_4$-PVA electrolyte. The ionic conductivity of 10 m $LiClO_4$-PVA OSGE is 1.32×10^{-2} $S\cdot cm^{-1}$ at room temperature. $Zn(ClO_4)_2$ is further added to $LiClO_4$-PVA OSGE to introduce Zn^{2+} ion conduction, which is optimized to 1 m $Zn(ClO_4)_2$+10 m $LiClO_4$-PVA and applied as the electrolyte in aqueous rechargeable Zn-Li hybrid batteries. The conductivity of Zn^{2+} ions is estimated as 5.31×10^{-3} $S\cdot cm^{-1}$ in the 1 m $Zn(ClO_4)_2$+10 m $LiClO_4$-PVA OSGE, which is high enough to be used as an electrolyte for batteries using Zn^{2+} ions as the charge carriers. The quasi-solid-state hybrid battery reaches a voltage of 2 V and delivers its highest discharge capacity and energy density as 116.6 $mAh\cdot g^{-1}$ and 183.3 $Wh\cdot kg^{-1}$ (calculated on the 5.6 mg active mass of $LiMn_2O_4$) respectively at first cycle,

becoming 93.5 $mAh \cdot g^{-1}$ and 138.0 $Wh \cdot kg^{-1}$ after 300 cycles with nearly 100% coulombic efficiency for the first 30 cycles before then becoming about 99% coulombic efficiency in the following cycles. OSGE is a useful strategy to develop aqueous electrolytes with wide electrochemical stability windows to be used as electrolytes for electrochemical devices.

1. INTRODUCTION

Li^+ ion batteries (LiBs) are the most popular type of batteries and have been widely used in portable and stationary applications, despite still facing challenges on safety, cost and environmental benignity. Conventional electrolytes based on $LiPF_6$, $LiCF_3SO_3$ and $LiBF_4$ salts and organic solvents such as propylene carbonate, ethylene carbonate, polyethylene oxide and dimethyl carbonate are expensive, environmentally unreliable and flammable[1-5]. Therefore, for large-scale applications especially for stationary grid electricity storage, aqueous rechargeable batteries (ARBs) are moving to the forefront due to their utilization of low-cost and safe water-based electrolytes, functioning as promising alternatives [6, 7]. Research in ARBs has extended the exploration from Li^+ ion intercalation materials to naturally abundant Na^+ and K^+ ion systems, to the intercalation chemistry of multivalent cations engaging in multiple electron transfer [8, 9]. Compared with the other divalent cation based ARBs, Zn^{2+} ion-based ARBs have obvious advantages including high abundance and large-scale production thereby making them inexpensive [9, 10]. Zinc is non-toxic, it has a low redox potential (-0.76 V vs. standard hydrogen electrode (SHE)), and has a good stability in water which is attributed to a high over-potential for hydrogen evolution reactions[11]. Therefore zinc is a suitable anode for aqueous rechargeable batteries.

However, owing to the narrow electrochemical stability window (1.23 V) of aqueous electrolytes, conventional Zn^{2+} ion-based ARBs have limited energy density and poor stability[12]. To handle these issues, many efforts regarding optimizing the compositions and structures of the cathodes have been introduced to improve the capacity of Zn^{2+} ion-based ARBs[13-16]. Alongside this, another method is attempting to get the quasi-solid-state ARBs by introducing poly(vinyl alcohol) (PVA) into the aqueous electrolytes to minimize the water content and provide a neutral pH medium and ameliorate the flexibility, wearability and stability of the full cells[17, 18]. Recently, a technical route of salt-concentrated electrolytes achieved by simply increasing the salt concentration in suitable salt-solvent combinations was proposed to broaden the stability windows of aqueous electrolytes and thus the energy density of full cells[19]. In addition, the concepts of 'water-in-salt' (WiS), 'water-in-bisalt' (WiBS) and hydrate-melt electrolytes which also meet the defination of salt-concentrated electrolytes were reported [20-23]. The WiSE reported by Wang and Xu's groups is typically prepared by dissolving lithium bis(trifluoromethane sulfonyl)imide (LiTFSI) at extremely high concentrations (molality >20 m, mol-salt in kg-solvent) in water, leading to an anion-containing Li^+ ion solvation sheath resulting in the formation of a dense interphase on the anode surface[21]. Combined with the dramatically reduced electrochemical activity of water at such a high concentration, the WiSE exhibited an outstanding electrochemical stability window of ~ 3.0 V [21]. In Yamada's research, lithium bis(pentafluoroethanesulfonyl)imide (LiBETI) and LiTFSI were selected and optimized to form an eutectic system as a room-temperature hydrate melt delivering an operating voltage of 3.1 V when utilized as the electrolyte for aqeous batteries[20]. However, the cost of expensive organic salts will limit the application of these salt-concentrated electrolytes in aqueous batteries. Therefore, it would be beneficial if these expensive organic salts

could be replaced by inexpensive inorganic salts. Aqueous solutions of salts such as nitrates and acetates have been investigated as the potential candidates for ARBs [24-26].

In this study, relatively cost-effective inorganic perchlorate salts have been used in the electrolytes for the preparation of quasi-solid-state ARBs, which have previously been utilized in conventional LiBs [27]. Aqueous solutions of salts such as $LiNiO_3$ and KOAc have been investigated as the potential electrolytes for ARBs [24-26, 28]. In reported papers on salt-concentrated aqueous electrolytes, the high concentration aqueous electrolytes were prepared at room temperature [20, 21, 24, 25, 29]. The wide electrochemical stability window of these electrolytes is closely related to the activity of water. A higher concentration of salt solution will lower the activity of solvent water thereby increasing the over-potential for the splitting of water into H_2 and O_2, leading to a widened electrochemical stability window. From this point of view, a processable crystal-type gel electrolyte for the application of supercapacitors is reported, exhibiting a wide operating voltage attributed to the crystallization of the salt and hydrophilic polymer[30]. Therefore, using an over-saturated aqueous solution of salts, with the addition of poly(vinyl alcohol) (PVA) for a gel electrolyte, which can also be referred to as 'over-saturated-gel electrolyte' (OSGE) is expected to further widen the electrochemical stability window. The water activity could be further reduced in OSGE by crystallizing the dissolved salts and solidifying the electrolytes, hence the electrochemical stability window is expected to be even wider. In this study, both 'room-temperature-saturated-gel electrolyte' (RTSGE) and OSGE using inorganic salt $LiClO_4$ as the ionic conductor were investigated. An electrochemical stability window of 2.7 V was observed for the 6 m $LiClO_4$-PVA RTSGE whilst the electrochemical stability window was further expanded to 3.3 V for the 10 m $LiClO_4$-PVA OSGE when the saturated $LiClO_4$ sol was prepared at 95°C

then slowly cooled down to room temperature. The stability window of that OSGE varied from 3.3 to 2.5 V when the temperature was increased from room temperature to 80°C, which demonstrates its potential capability as the electrolyte in ARBs operated at elevated temperatures. Crystals were observed at room temperature in the OSGE, but its high ionic conductivity of 1.32×10^{-2} $S\cdot cm^{-1}$ at room temperature is sufficient to be used as an electrolyte for batteries. The addition of PVA facilitates the homogeneous distribution of the un-ionised $LiClO_4$ in the OSGE when cooled down to lower temperatures, which is analogous to a dispersed phase, when compared with dissolved $LiClO_4$ and PVA involved in hydrogel (continuous phase), therefore maintaining the desired conductivity while reduced the activity of water. There is a noticeable increase in viscosity of the aqueous electrolytes if too much PVA is used thereby decreasing the ionic conductivity. However, it may fail to form a continuous phase and evenly disperse the crystal $LiClO_4$ if insufficient PVA is added. Therefore, according to previous work, the amount of PVA is determined as 10wt% versus the mass of solvent[23, 31-33]. The electrochemical stability window was basically retained at 3.0 V when 1 m $Zn(ClO_4)_2$ was added into this OSGE to introduce the Zn^{2+}-ion conductivity. The conductivity of Zn^{2+} ions in that OSGE was estimated as 5.31×10^{-3} $S\cdot cm^{-1}$ by a current interruption method.

Hybrid ion ARBs have attracted much attention from researchers. Unlike the traditional 'rocking-chair' LiBs functioning on the basis of the immigration of Li ions between cathode and anode, hybrid ion ARBs involve the immigration of more than one type of ions between the electrolyte and each electrode, therefore integrating the advantages of various single ion ARBs[7, 34]. Compared with single ion ARBs, hybrid ion ARBs have been receiving extensive interest owing to their higher operating voltage and energy density [35-37], among which the rechargeable aqueous

$Zn/LiMn_2O_4$ battery proves to be a very promising hybrid ion ARB for energy storage [38-40]. Our hybrid Zn-Li battery exhibits a higher operation voltage than popularly used aqueous Zn ion batteries[41], demonstrating the wide stability window of the OSGE used. Based on this novel inexpensive 1 m $Zn(ClO_4)_2$+10 m $LiClO_4$-PVA OSGE, a rechargeable hybrid battery was prepared, with zinc foil as the anode, and $LiMn_2O_4$ on Ti mesh as the cathode. During charge-discharge cycling, the coulombic efficiencies (CEs) were nearly 100% during the first 30 cycles retaining at around 99.0% in the following cycles. A discharge capacity of 116.6 $mAh \cdot g^{-1}$ and an energy density of 183.3 $Wh \cdot kg^{-1}$ for first cycle were delivered, which became 93.5 $mAh \cdot g^{-1}$ and 138.0 $Wh \cdot kg^{-1}$ with 79.1 % capacity retention after 300 cycles.

2. EXPERIMENTAL SECTION

2.1 Fabrication of 'over-saturated-gel' electrolyte (OSGE)

The electrolyte (1 m $Zn(ClO_4)_2$+10 m $LiClO_4$-PVA) was prepared by dissolving $Zn(ClO_4)_2 \cdot 6H_2O$ (Alfa Aesar, Reagent Grade) and $LiClO_4$ (Alfa Aesar, 98%) in deionized water at 95°C according to the molality (m, molar of dissolved salts in 1 kg solvent) to get the over-statured aqueous solution, this was followed by adding 10 wt.% poly(vinyl alcohol) (PVA) (Sigma-Aldrich, 99+% hydrolyzed) vs. the solvent and vigorously stirring for 5 hours at 95 °C to obtain a homogeneous aqueous sol before cooling down to room temperature forming a quasi-solid-state aqueous gel.

2.2 Assembly of $Zn/LiMn_2O_4$ coin cell

$LiMn_2O_4$ power was synthesized by dispersing calculated amounts of MnO_2 (Alfa Aesar, 99.9%) and LiOH (Sigma Aldich, 99%) in ethanol. The ethanol was slowly evaporated at room temperature under stirring. The obtained mixture was manually ground in an agate mortar and pestle for 10 minutes and then put in an alumina crucible and calcined in air at 800 ºC for 20 hours[42]. The as-prepared $LiMn_2O_4$ sample was mixed with Super P and polytetrafluoroethylene (PTFE) with the mass ratio of 85:10:5, then tape cast on a titanium (Ti) mesh. The active mass can be controlled at around 5-6 mg on the Ti mesh with a 12 mm diameter. Commercial zinc foil was polished by zinc powder (Alfa Aesar, median 6-9 micron, 97.5%) for around 15 min, followed by washing with soap and deionized water, rinsing with 2-proponal and finally drying at 60°C in a vacuum oven for 3 h[43]. Meanwhile, the OSGE was heated on the hot plate at 95°C to be converted into the flexible sol state before being cast on the glass microfiber filters (Whatman). It is turned into quasi-solid state after cooling down to room temperature. Zn anode and $LiMn_2O_4$-Ti mesh cathode were cut into round shape discs with 12 mm diameter using a precision disc cutting machine (Kejing, MSK-T10), while the electrolyte was cut into a 16 mm-diameter disc. Finally, the anode, cathode and electrolyte were assembled together in the CR2016 coin cell using a hydraulic crimping machine (Kejing, MSK-110).

2.3 Material Characterization

Thermo Scientific STAR A214 pH meter was employed to test pH values of different aqueous solutions with various salt concentrations. The X-ray diffraction (XRD) data was collected on a PANanalyticalX'Pert Pro in the Bragg-Brentano reflection geometry with a Ni-filtered Cu Kα source (1.5405 Å), fitted with the X'Celerator detector and an Empyrean CuLFF xrd tube. Absolute scans in the 2θ range of 10–90° with step sizes of 0.0167° were used during data collection. Scanning electron microscopy (SEM) measurements were carried out on a ZEISS

SUPRA 55-VP Field Emission Scanning Electron Microscope equipped with an energy dispersive X-ray (EDX) spectrometer that allows elemental composition analysis. Simultaneous thermal analysis (STA) was conducted using a NETZSCH STA 449 F3-Jupiter Thermal Analyser on heating from room temperature to 600 °C in air, with a heating rate of 10 °C/min and a flow rate of compressed air of 50 $mL \cdot min^{-1}$. Fourier-transform infrared spectroscopy (FTIR) measurements were carried out on a Bruker Vertex 70V IR spectrometer.

2.4. Electrochemical measurements

To test the electrochemical stability windows of electrolytes, two Ti foils which had been ultrasonically washed in 2-propanol before, were inserted into the heated electrolyte as the working electrode and counter electrode, whilst Ag/AgCl was used as the reference electrode. A Solartron 1470E multichannel cell test system was employed to test linear sweep voltammetry (LSV) curves of the electrolytes. Electrochemical impedance spectroscopy (EIS) was employed to obtain the ionic conductivity of various electrolytes through an integrated Solartron 1455A or Solartron 1287A frequency response analyzer with 10 mV bias and 1 M-0.1 Hz for 1455A or 100 k-0.1 Hz for 1287A frequency range. The conductivity cell constants were predetermined using 0.1 m aqueous KCl standard solution at 25°C. To determine the ionic conductivity of Zn^{2+} ions in 1 m $Zn(ClO_4)_2$+10 m $LiClO_4$ OSGE containing mixed charge carriers, current interrupt method was utilized with 1.0 V vs. Zn/Zn^{2+} applied voltage to the Zn/Zn symmetric cell based on OSGE. In comparison of the resistance of the OSGE and 0.1 m KCl standard solution with the same geometric factor, the ionic conductivity of Zn^{2+} ion can be estimated. All the cyclic voltammetry (CV) curves were collected by a Solartron 1470E multichannel cell test system under 1 $mV \cdot s^{-1}$ scanning rate. Assembled Zn|1 m $Zn(ClO_4)_2$+10 m $LiClO_4$-PVA|Ti mesh-$LiMn_2O_4$ CR2016 coin

cells were relaxed under a prescribed cut-off condition for 8 h until they obtained a relative equilibrium condition. After that, galvanostatic charge-discharge cycling with potential limitation (0.8-2.0 V vs. Zn/Zn^{2+}) were carried out using Land BT2000 battery test system at room temperature.

3. RESULTS AND DISCUSSION

3.1. Properties of OSGE

When investigated as a salt of electrolytes for Li-O_2 batteries, $LiClO_4$ usually perform better (greater discharge capacity) than LiTFSI-containing electrolytes. This is attributed to the better solvent viscosity, oxygen solubility and stability against oxygen[27, 44, 45]. However, for ARBs, $LiClO_4$ or any other perchlorates are seldom used as the salts in electrolytes due to safety and toxicity concerns[27]. For this reason, PVA is utilized by us to consolidate the perchlorates in the quasi-solid-state electrolyte[31]. In order to investigate the advantages of the OSGE, the electrochemical stability windows of 1 m (unsaturated), 6 m (RTSGE) and 10 m (OSGE) $LiClO_4$-PVA are shown in Fig. 1a. The electrochemical stability window for unsaturated 1 m $LiClO_4$-PVA gel electrolyte is 2.3 V (-0.6 to 1.7 V vs. Ag/AgCl). Further increasing the concentration of $LiClO_4$ until saturated at room temperature (6 m), the electrochemical stability window increased to 2.7 V (-0.9 to 1.7 V vs. Ag/AgCl). In order to maximise the electrochemical window, $LiClO_4$-PVA OSGE was prepared by dissolving the $LiClO_4$ at 95 °C until it is saturated at this temperature. After cooling down to room temperature, the obtained electrolyte is referred to as OSGE. The

electrochemical window of 10m $LiClO_4$-PVA OSGE is 3.3 V (-1.4 to 1.9 V vs. Ag/AgCl), which is 1.0 V higher than the unsaturated 1 m $LiClO_4$-PVA electrolyte and 0.6 V higher than the normal saturated 6 m $LiClO_4$-PVA electrolyte. Meanwhile, the electrochemical window of 10 m $LiClO_4$ over-saturated aqueous solution without PVA was 2.9 V (-1.1 to 1.8 V vs. Ag/AgCl) at a scanning rate of 1 $mV \cdot s^{-1}$ (Supporting Information, Fig. S1), which is 0.4 V less than that with added PVA. This means that the addition of PVA also helps to expand the electrochemical stability window [31]. Fig. 1b shows the electrochemical stability window of 10 m $LiClO_4$-PVA OSGE at different scanning rates. When the scanning rate is increased from 1 to 50 $mV \cdot s^{-1}$, the cut-off potential for both the reduction side and oxidation side of the windows can be basically maintained. However, at the oxidation side, the reversible non-Faradaic current at a low scanning rate of 1 $mV\ s^{-1}$ is much smaller than those at a scanning rate at or above 5 $mV\ s^{-1}$ [46]. This could be related to the slow diffusion of large ClO_4^- ions towards the working electrode, Ti foil, at this low scanning rate. Although the observed current at the oxidation onset in Fig. 1b increases with the raise of scanning rate, it is believed that this is due to the reversible non-faradaic (capacitive) current which contributes relatively low influence to stability window compared to the faradaic current[46]. The variation of the stability window of 10 m $LiClO_4$-PVA OSGE versus temperature from room temperature to 80°C is recorded in Fig. 1c, which exhibits the stability window as 3.3 V (-1.4 to 1.9 V vs. Ag/AgCl) at room temperature, 3.0 V (-1.3 to 1.7 V vs. Ag/AgCl) at 40°C, 2.8 V (-1.2 to 1.6 V vs. Ag/AgCl) at 60°C, and 2.5 V (-1.0 to 1.5 V vs. Ag/AgCl) at 80°C. The reduced electrochemical stability window could be caused by the decreased over-potential for the oxygen and hydrogen evolution reactions on the two electrodes at elevated temperatures. In Fig. 1d, the optical image of reversible transition between sol and gel state for the OSGE at 95 °C and room

temperature can be observed, further demonstrating the wide range of operating temperatures of this OSGE.

Besides wide electrochemical stability windows, sufficient ionic conductivity is another important parameter for battery electrolytes. Therefore the ionic conductivities of the 1 m , 6 m and 10 m $LiClO_4$-PVA gel electrolytes were measured by a.c. electrochemical impedance spectroscopy (EIS) using 0.1 m KCl aqueous solution (conductivity 1.28×10^{-2} $S\cdot cm^{-1}$ at room temperature) as the calibration solution [47]. The impedance responses of the three samples are shown in Supporting Information, Fig. S2, with the corresponding ionic conductivity of the samples listed in Supporting Information, Table S1. The total conductivity of 1 m and 6 m $LiClO_4$-PVA electrolytes is 4.31×10^{-2} $S\cdot cm^{-1}$ and 9.9×10^{-2} $S\cdot cm^{-1}$ respectively. The ionic conductivity enhances with increased $LiClO_4$ concentration due to there being more charge carriers present in the concentrated salt solution. As for the 10 m $LiClO_4$-PVA OSGE, the conductivity decreased to 1.32×10^{-2} $S\cdot cm^{-1}$ at room temperature, which is lower than the 1 m unsaturated $LiClO_4$-PVA gel electrolyte. It is believed that the OSGE contains extra salts in the gel electrolyte, thus strong interactions between these extra salts and solvent water will reduce the activity of solvent water widening the electrochemical stability window. This interaction will also reduce the ionisation of $LiClO_4$, thus the effective concentration of charge carriers will be reduced leading to decreased ionic conductivity. Nevertheless, PVA in $LiClO_4$-H_2O-PVA gel helps the homogenous distribution of the salt, which is usually utilized as the disperser for sol-gel processing to disperse the crystals evenly and realize the reversible transition between sol and gel state[48] so that the un-ionised small $LiClO_4$ crystals are isolated by the continuously conductive phase thus retaining high conductivity. To prove this function of PVA, the ionic conductivity of 10 m $LiClO_4$ electrolyte without PVA is tested and

shown in Fig. S2, which is 9.90×10^{-3} S·cm^{-1}, lower than that of the 10 m $LiClO_4$ electrolyte with PVA, this value is consistent with previous research on PVA-based gel electrolytes [48]. This explains why the ionic conductivity of 10 m $LiClO_4$-PVA OSGE is still much higher than that of the most popular solid state electrolytes used in conventional batteries.[49] In addition, the ionic conductivity of 10 m $LiClO_4$-PVA OSGE increases from 1.32×10^{-2} to 1.86×10^{-1} S·cm^{-1}, when the temperature increases from room temperature to 80°C (Fig. 1e), providing an advantage to OSGE for batteries operating at evaluated temperatures.

In order to use the 10 m $LiClO_4$-PVA OSGE in an aqueous rechargeable hybrid battery using Zn as the anode, it is necessary to introduce Zn^{2+} ion conduction. Owning to the similar chemical properties with $LiClO_4$, $Zn(ClO_4)_2$ was added to induce Zn^{2+} ions and combined with $LiClO_4$ to form an OSGE (over-saturated for $LiClO_4$ and unsaturated for $Zn(ClO_4)_2$). However, according to previous reports, the pH values of aqueous electrolytes can significantly affect their performance[50]. It is therefore necessary for us to optimize the concentration of added $Zn(ClO_4)_2$ based on the pH values of aqueous solutions. In Fig. 2a, the pH value of room temperature-saturated 3 m $Zn(ClO_4)_2$ and 1 m $Zn(ClO_4)_2$ aqueous solution are 1.02 and 3.44 respectively. The acidic environment formed due to the hydrolysis of Zn^{2+} ions enhances the activity towards the hydrogen evolution reaction[50]. However, when the $LiClO_4$ concentration is increased, the pH value increases accordingly finally reaching 5.38 for 1 m $Zn(ClO_4)_2$ + 6 m $LiClO_4$, which is a weak acid. With the addition of PVA, the RTSGE approaches neutrality with a pH value of 6.25. Although, the pH meter employed in our lab cannot detect the pH value of OSGE with semi-solid state, it is believed that the pH value can approach neutrality due to the addition of more $LiClO_4$, suppressing the hydrolysis of Zn^{2+} ions. Therefore the activity for the hydrogen evolution reaction will be further

decreased[50]. The pH value is higher when a lower concentration of $Zn(ClO_4)_2$ (1 m) was added, thus the concentration of $Zn(ClO_4)_2$ added in 10 m $LiClO_4$-PVA OSGE was fixed to 1 m. To further demonstrate the advantages of 1 m $Zn(ClO_4)_2$+10 m $LiClO_4$-PVA OSGE, 1 m $Zn(ClO_4)_2$-PVA, 3 m $Zn(ClO_4)_2$-PVA, 1 m $Zn(ClO_4)_2$ + 6 m $LiClO_4$-PVA and 1 m $Zn(ClO_4)_2$+10 m $LiClO_4$-PVA electrolytes were prepared for comparison. As shown in Fig. 2b, 1 m $Zn(ClO_4)_2$+10 m $LiClO_4$-PVA OSGE is stable within the voltage range of -1.3 to 1.7 V vs. Ag/AgCl under an scanning rate of 1 $mV \cdot s^{-1}$. However, the other three electrolytes show relatively narrow windows of -1.0 to 1.1, -0.8 to 1.4 and -1.0 to 1.6 V respectively. The EIS patterns of these electrolytes are shown in Supporting Information, Fig. S3. The electrochemical stability windows and ionic conductivity of all these electrolytes are summarized in Supporting Information, Table S1. The ionic conductivity of 1 m $Zn(ClO_4)_2$+10 m $LiClO_4$-PVA electrolyte is 8.51×10^{-3} $S \cdot cm^{-1}$ which is lower than that of 1 m $Zn(ClO_4)_2$-PVA (7.27×10^{-3} $S \cdot cm^{-1}$), 3 m $ZnClO_4$-PVA (1.09×10^{-2} $S \cdot cm^{-1}$) and 1 m $Zn(ClO_4)_2$+6 m $LiClO_4$-PVA electrolyte (2.20×10^{-2} $S \cdot cm^{-1}$). Moreover, the measured conductivity of 1 m $Zn(ClO_4)_2$+10 m $LiClO_4$-PVA OSGE by EIS is the total conductivity which included the conductivity of all the charge carriers such as Li^+, Zn^{2+}, ClO_4^- ions. In order to estimate the conductivity of Zn^{2+} ions, the current interrupt method was employed in the same set-up and dimension as the 0.1 m KCl standard solution using Zn foil as both the work and counter electrodes. These Zn foils are reversible electrodes for Zn^{2+} ions while they are blocking electrodes for other ions. As shown in Fig. 2c, after applying 1.0 V vs. Zn/Zn^{2+} voltage, the current drops due to this blocking effect from the Zn foil electrodes to ions other than Zn^{2+} in the OSGE, after this the current remains stable around 9.8 mA to the end. The ohmic resistance caused by Zn^{2+} ion migration can be estimated as 102.0 Ω, hence the ionic conductivity of Zn^{2+} ions in 1 m $Zn(ClO_4)_2$+10 m $LiClO_4$-PVA OSGE can be estimated as 5.31×10^{-3} $S \cdot cm^{-1}$, which is high enough

to be used as an electrolyte for Zn^{2+}-ion batteries. Considering both the electrochemical stability window and ionic conductivity, 1 m $Zn(ClO_4)_2$+10 m $LiClO_4$-PVA OSGE is a suitable electrolyte for Zn-Li hybrid batteries.

To demonstrate the feasibility of Zn plating/stripping with these electrolytes, Zn symmetric cells were assembled in CR2016 coin cells, and tested using cyclic voltammetry (CV) under 1 $mV \cdot s^{-1}$ scanning rate within the potential range of -0.6 to 0.6 V vs. Zn/Zn^{2+}. As shown in Fig. 2d, the symmetric peaks of oxidation and reduction of the Zn symmetric cell with 1 m $Zn(ClO_4)_2$+10 m $LiClO_4$-PVA electrolyte from the 1st to 5th CV scanning can be observed around 0.2 and -0.2 V, which demonstrates stable Zn plating/stripping. The other three electrolytes, 1 m $Zn(ClO_4)_2$, 3 m $Zn(ClO_4)_2$ and 1 m $Zn(ClO_4)_2$ + 6 m $LiClO_4$-PVA, display unstable CV curves under the same condition as shown in Supporting Information, Fig. S4. Meanwhile through the chronocoulometry curves based on the CV curves, all the CEs of these Zn symmetric cells within 5 cycles are less than 70%. This is much lower than when 1 m $Zn(ClO_4)_2$ + 10 m $LiClO_4$-PVA OSGE was used reaching over 98%(Fig. S5). The relatively narrow stability windows of these electrolytes can be related to the observed unstable CV curves, while the pH values of these three electrolytes are expected to be lower than that of OSGE, which facilitates hydrogen evolution reactions due to the high concentration of protons, thus reducing the electrochemical stability window. The Zn symmetric cell based on the 1 m $Zn(ClO_4)_2$ + 10 m $LiClO_4$-PVA OSGE was conducted for galvanostatic charge-discharge cycling under 5 $mA \cdot cm^{-2}$ current density with potential limitation from -0.2 to 0.2 V vs. Zn/Zn^{2+} (Fig. S5). The CE of that cell in first cycle was 3.8% due to the OCV (-0.12 V) becoming 92.9% and maintained above 98% after first the 10 cycles even reaching above 99% at certain cycles, indicating OSGE can significantly improve the CE of Zn

plating/stripping. After this test, the cell was separated, and the obtained Zn foil was characterized by SEM with its SEM image of 2.5 μm resolution shown in Supporting Information, Fig. S6. No dendrite was observed on the Zn foil. Dendrite growth at the Zn anode is therefore suppressed in the OSGE.

In order to characterize 1 m $Zn(ClO_4)_2$+10 m $LiClO_4$-PVA OSGE, Fourier transform infrared spectroscopy (FTIR) was employed to identify its composition and liquid structure (Fig. 3a). For comparison, all the original chemicals present in the electrolyte were also tested (Supporting Information, Fig. S7). In the curve corresponding to PVA powder, a broad band in the range of 3600–3100 cm^{-1} is observed and ascribed to O-H stretching vibrations, which can also be seen in the curve of the electrolyte due to the existence of water as well as the curve of $Zn(ClO_4)_2 \cdot 6H_2O$ due to the existing of crystallised water, while its band at 2950–2910 cm^{-1} is attributed to the asymmetric and symmetric stretching modes of $-CH_2-$ groups[51]. The peaks at 1431 and 1338 cm^{-1} which also exist in the curve of electrolyte as two weak peaks, are attributed to the bending mode of $-CH_2-$[51]. The peaks of $Zn(ClO_4)_2 \cdot 6H_2O$, $LiClO_4$ and OSGE on ClO_4^- symmetric and asymmetric stretching band are present at ~1050 cm^{-1} and ~1610 cm^{-1} respectively[52]. The peaks in the curve of all the electrolytes in Fig. 3a reflects the peaks of all the original chemicals. 1 m $LiClO_4$-PVA, 6 m $LiClO_4$-PVA and 10 m $LiClO_4$-PVA electrolytes have been characterized by FTIR in Fig. 3a in order to explain the further extended stability window of OSGE over RTSGE. Noticeably, in the curve of OSGE, the peak of the hydrogen bond around 3310 cm^{-1} shrinks and the two peaks at ~3550 and 3590 cm^{-1} corresponding to $LiClO_4$ become sharper, compared with the RTSGE and indicating the solidification of OSGE, which can suppress the activity of water attributing to the hydrophilic polymer and quasi-solid state, thence widen the stability windows[53]. Thermal gravimetric analysis (TGA) and differential scanning calorimetry (DSC) analysis were utilized to

characterize the thermal property of the 1 m $Zn(ClO_4)_2$+10 m $LiClO_4$-PVA OSGE (Fig. 3b). The first peak of the DSC curve occurs at ~110°C, this corresponds to the phase transition of electrolyte from quasi-solid state to liquid state, before that the weight loss in the TGA curve is mainly due to the evaporation of water. After that, an acceleration of weight loss in the TGA curve was observed due to the decomposition of PVA. A further, faster weight loss and another peak in the DSC curve around 220°C is likely due to the decomposition of perchlorates[54]. However, the fastest weight loss of 10 m $LiClO_4$-PVA OSGE happens at a temperature around 280°C (Supporting Information, Fig. S8) owing to the higher decomposition temperature of $LiClO_4$ compared to that of $Zn(ClO_4)_2$ [55]. To demonstrate the appearance of that OSGE furthermore, the optical image of its top side is provided in Supporting Information, Fig. S9, which is a transparent sol. The optical image of OSGE cast on glass microfiber filter and cut into a round disc with 16 mm diameter disc is shown in Fig. 3c, which displays quasi-solid state. The scanning electron microscope (SEM) image of that electrolyte with 37 X magnification is also shown in Fig. 3d. There are some dents on the surface of electrolyte in Fig. 3d. For SEM pictures with high magnification, there are some small pores (Supporting Information, Fig. S10a), which could be attributed to the loss of water in the electrolyte under the high vacuum of the SEM measurement environment. The mappings of elements O, Zn, C and Cl (Supporting Information, Fig. S10b, c, d and e) demonstrate the homogeneous distribution of these elements.

3.2. Properties of aqueous rechargeable Zn-Li hybrid battery based on OSGE

As the 1 m $Zn(ClO_4)_2$+10 m $LiClO_4$-PVA OSGE can conduct both Li^+ and Zn^{2+} ions, we are able to take advantage of both Li^+ and Zn^{2+} ionic conduction to make hybrid Zn-Li batteries. In our Zn|1 m $Zn(ClO_4)_2$+10 m $LiClO_4$-PVA|$LiMn_2O_4$-Ti mesh hybrid battery, the well-established Li^+ ion insertion/extraction happens at the $LiMn_2O_4$ cathode in a highly reversible manner, whereas

Zn strips/plates at the Zn anode. The corresponding XRD pattern of prepared $LiMn_2O_4$ powder for the cathode is shown in Supporting Information, Fig. S11, which exhibits the single phase of $LiMn_2O_4$ (ICDD: 01-070-8343). In Fig. 4a, two pairs of oxidation/reduction peaks occur at ~1.0/~0.9 V vs. Ag/AgCl (4.26 and 4.16 V vs. Li/Li^+) and ~ 0.9/~0.75 V vs. Ag/AgCl (4.16 and 4.01 V vs. Li/Li^+) respectively, indicating the insertion/extraction reaction of Li^+ ions in $LiMn_2O_4$[56]. The other pair of redox peaks happen at ~-0.75 and ~-1.1 V vs. Ag/AgCl (~0.23 and ~-0.12 V vs. Zn/Zn^{2+}), representing the Zn plating/striping[57]. In Fig. 4b, a galvanostatic cycling test of 300 cycles was obtained under 1 C (148 $mA \cdot g^{-1}$) charge/discharge rate within the voltage range of 0.8 to 2.0 V vs. Zn/Zn^{2+}, while the corresponding galvanostatic charge-discharge curves are exhibited in Fig. 4c. In the first cycle, the charge and discharge capacity of the cell is 118.2 and 116.6 $mAh \cdot g^{-1}$ respectively (calculated on the basis of 5.6 mg active mass of $LiMn_2O_4$) and its CE can be determined as 98.7%. After that, during the continuous charge-discharge process, its CE is retained nearly 100% for the first 30 cycles and about 99% in the following cycles to 98.8% at the 300^{th} cycle, with 94.6 $mAh \cdot g^{-1}$ charge capacity, 93.5 $mAh \cdot g^{-1}$ discharge capacity and 79.1% capacity retention in the last cycle compared to the first cycle (also the cycle with highest capacity). Nearly 100% CEs were also achieved in aqueous electrolytes based on organic salts such as lithiumbis(trifluoromethane sulfonyl)imide (LiTFSI) or 1 m $Zn(TFSI)_2$ + 20 m LiTFSI electrolyte [21, 29]. To the best of our knowledge, nearly 100% CE has not been observed in aqueous batteries based on inorganic salt electrolytes. This $Zn/LiMn_2O_4$ quasi-solid-state aqueous battery based on OSGE is a half-cell involving a Zn foil anode, thus the capacity and energy density are calculated based on the mass of $LiMn_2O_4$. Compared with $Zn/LiMn_2O_4$ half-cells based on the other electrolytes, the maximum capacity of our $Zn/LiMn_2O_4$ cell (116.6 $mAh \cdot g^{-1}$) is impressive, with a value higher than that reported in other hybrid $Zn\text{-}LiMn_2O_4$ batteries [58-60]. However, a fast capacity

decay was observed for the initial 30 cycle, which may be caused by the phase transition of $LiMn_2O_4$ from cubic Ⅰ to cubic Ⅱ [61] and/or the agglomeration of $LiMn_2O_4$ particles, being demonstrated in the SEM characterization in Fig. 6. Moreover, the EIS characterization for the cell before and after electrochemical testing in Fig. S12 indicates that the resistance of both electrolyte and interface between electrode and electrolyte decreases, revealing improved interfacial contacts after the electrochemical tests. In other electrochemical devices such as proton exchange membrane fuel cells (PEMFCs) or solid oxide fuel cells, activating the electrochemical cells by passing a small current across the cell will improve the electrolyte/electrode interfaces thus the series and total resistances of the electrochemical cells decreased [62, 63]. This may also happen in our cells based on OSGE, similar to the electrolytes in PEMFCs. Its energy density (obtained by integrating the discharge curve) can be calculated as 183.3 $Wh \cdot kg^{-1}$ for the first cycle and 138.0 $Wh \cdot kg^{-1}$ for the 300^{th} cycle. Furthermore, the rate performance of that coin cell was tested under C-rate of 1, 2, 4, 6 and 8 respectively (Fig. 4d), with corresponding specific charge/discharge capacities of the last cycle under certain current densities determined as 94.0/92.9, 81.8/81.1, 68.7/68.3, 53.8/53.3 and 41.5/41.2 $mAh \cdot g^{-1}$. After the charge/discharge rate was returned to 1 C, the charge/discharge capacity became 88.5/87.8 $mAh \cdot g^{-1}$ at the last charge/discharge cycle.

3.3. Characterization on the components of coin cell before and after electrochemical test

After the electrochemical test, the coin cell was separated, with the optical images of different components shown in Supporting Information, Fig. S13a, b and c. As shown in Supporting Information, Fig. S13d, FTIR spectra of the OSGE before and after electrochemical tests are almost unchanged indicating the electrolyte is fairly stable. As shown in Fig. 5a, the layered

mapping of Ti mesh-$LiMn_2O_4$ electrodes before and after the electrochemical test are compared. It has been observed that the particle size of $LiMn_2O_4$ increased after the electrochemical test. The agglomeration of $LiMn_2O_4$ particles may affect the insertion/desertion of Li^+ ions, leading to the slowly decreased capacity during the charge/discharge process. The existence of elements Zn and Cl in the layered mapping of the $LiMn_2O_4$ electrode after the cycling test is due the contact with perchlorate-based OSGE. The corresponding mappings of the individual elements in the $LiMn_2O_4$ cathode are shown in Supporting Information, Fig. S14 and S15 for samples before and after the electrochemical test respectively. In Fig. 5b, the XRD patterns of the Ti mesh-$LiMn_2O_4$ electrodes before and after the electrochemical test are compared as well. $LiMn_2O_4$ (ICDD: 01-070-8343) can be detected in both XRD patterns as the main phase. Carbon peaks can be found in both patterns due to the existence of carbon conductivity addition (Super P), while $Zn(ClO_4)_2$ can only be observed in the sample after the electrochemical test. In Fig. 5c, the XRD patterns of Zn foil anodes before and after the electrochemical test are compared, both are composed of Zn (ICDD: 04-008-6027). The SEM image of the Zn foil anode before the electrochemical tests with a smooth surface are observed under different magnifications in Supporting Information, Fig. S16. The cross section of the Zn anode after cycling is shown in Fig. 5d, combining with the layered mapping of the Zn anode in Fig. 5e. No dendrite was observed on the Zn anode at the cross-section after the electrochemical test. For rechargeable Zn^{2+}-ion batteries, dendrites induced by the uneven metal deposition on the anode can lead to thermal runaway and explosion hazards, which is an obstacle for commercialisation of batteries[64]. In our hybrid battery, the high salt concentration can increase the threshold critical current density for cations becoming depleted in the electrolyte thus suppressing the formation of zinc dendrites[64], which significantly improves the safety of this

battery. A dendrite-free Zn anode was also observed in rechargeable aqueous Zn^{2+}-ion batteries based on WiBS with high salt concentration[29].

4. CONCLUSIONS

In this study, for the first time, the use of OSGE further expands the electrochemical stability window of aqueous electrolytes in order to be used in electrochemical energy storage devices such as batteries or super-capacitors to achieve a higher energy density. Compared to expensive organic salts, low-cost inorganic salt $LiClO_4$ is used in the OSGE with a similar electrochemical stability window achieved. The electrochemical stability window of 6 m RTSGE $LiClO_4$-PVA reaches 2.7 V, while it is extended to 3.3 V, when the electrolyte is prepared as saturated (10 m) at 95 ^oC and then cooled down to room temperature forming as an OSGE. With the addition of PVA, the un-ionised $LiClO_4$ crystals are homogeneously dispersed in the gel electrolyte. Due to mixed charge carriers in OSGE, the conductivity of Zn^{2+} ions is evaluated by the current interrupt method. The properties of this OSGE at evaluated temperature have been investigated as well. It has a stable electrochemical window of 2.5 V and ionic conductivity of 1.86×10^{-1} $S\cdot cm^{-1}$ at 80 °C. To optimize the composition of OSGE containing $LiClO_4$ and $ZnClO_4$ for hybrid batteries, the pH value, electrochemical windows, and ionic conductivity are jointly investigated on electrolytes with various $Zn(ClO_4)_2$ to $LiClO_4$ ratios. It is identified that 1 m $Zn(ClO_4)_2$+10 m $LiClO_4$-PVA OSGE is an ideal electrolyte for aqueous rechargeable hybrid Li-Zn batteries. Finally, the Zn anode and $LiMn_2O_4$-Ti mesh cathode with OSGE were assembled together in a coin cell with a voltage of 2.0 V. It delivers its highest discharge capacity and energy density as 116.6 $mAh\cdot g^{-1}$ and 183.3 $Wh\cdot kg^{-1}$ (calculated on the 5.6 mg active mass of $LiMn_2O_4$) respectively at first cycle, becoming 93.5

$mAh \cdot g^{-1}$ and 138.0 $Wh \cdot kg^{-1}$ at 300 cycles with close to nearly 100% coulombic efficiency for the first 30 cycles then retained to about 99% coulombic efficiency in the following cycles. During the charge-discharge test on that coin cell, the CE is kept around 100% at the first 30 cycles then retained around 99%. After cycling, the anode, cathode and OSGE are examined through XRD, SEM, EDX, STA and FTIR, whist the Zn anode is dendrite-free. Agglomeration of $LiMn_2O_4$ particles is observed after the electrochemical test, which may be related to the slow decrease in capacity. The above attempts demonstrate a viable route to apply OSGE in ARBs, with the potential to be operated above room temperature. The strategy on using OSGE with a wide electrochemical stability window has been successfully extended to other salts, which will be reported in future papers.

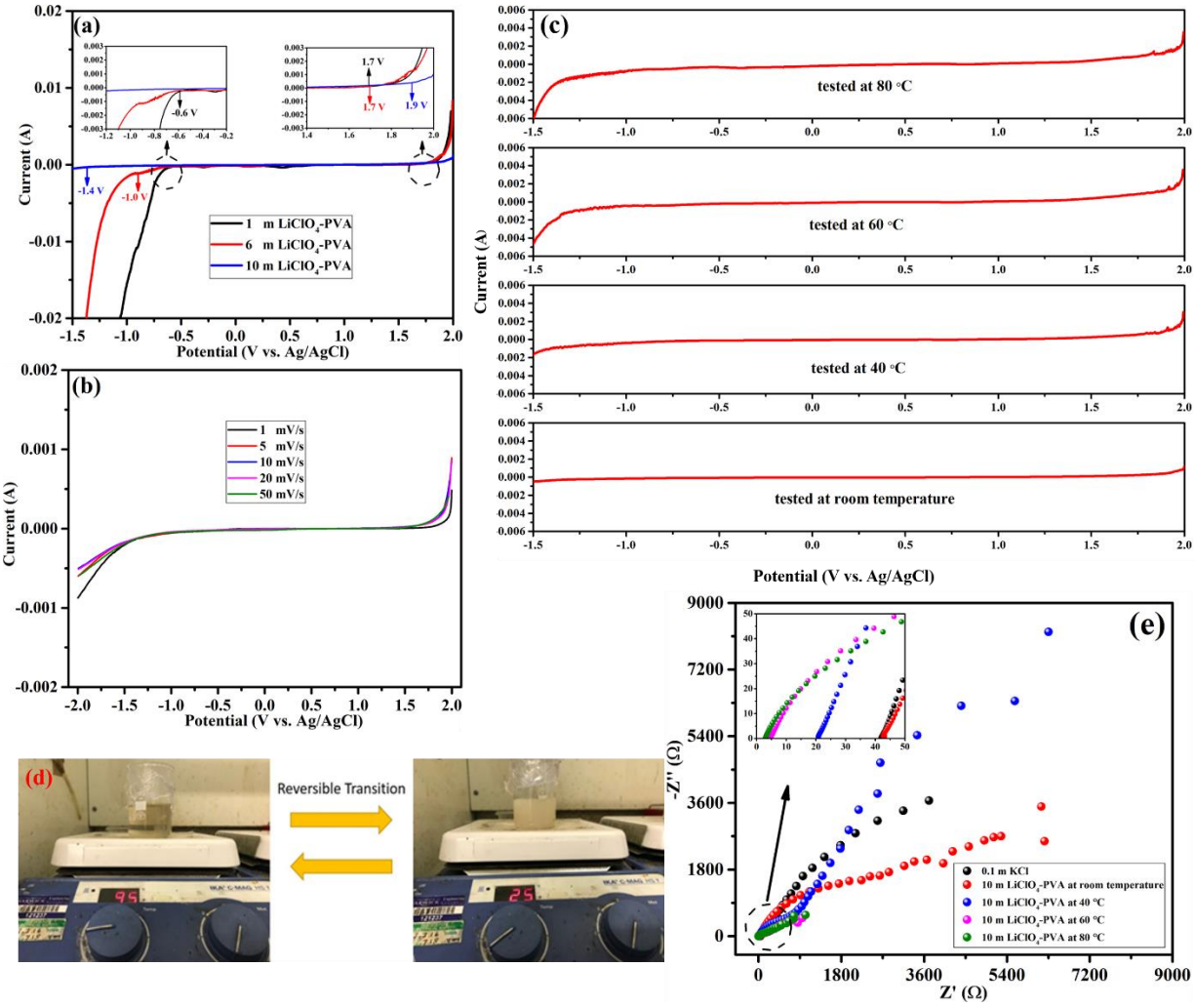

Figure 1. Stability window test on 1, 6 and 10 m $LiClO_4$-PVA electrolyte under 1 $mV \cdot s^{-1}$ (a); Stability window test on 10 m $LiClO_4$-PVA OSGE under different scanning rates (b); Stability widow test on 10 m $LiClO_4$-PVA OSGE at various temperatures (c); Optical image on reversible transition between sol and gel state of 10 m $LiClO_4$-PVA OSGE (d); EIS test on 10 m $LiClO_4$-PVA OSGE at various temperatures (e).

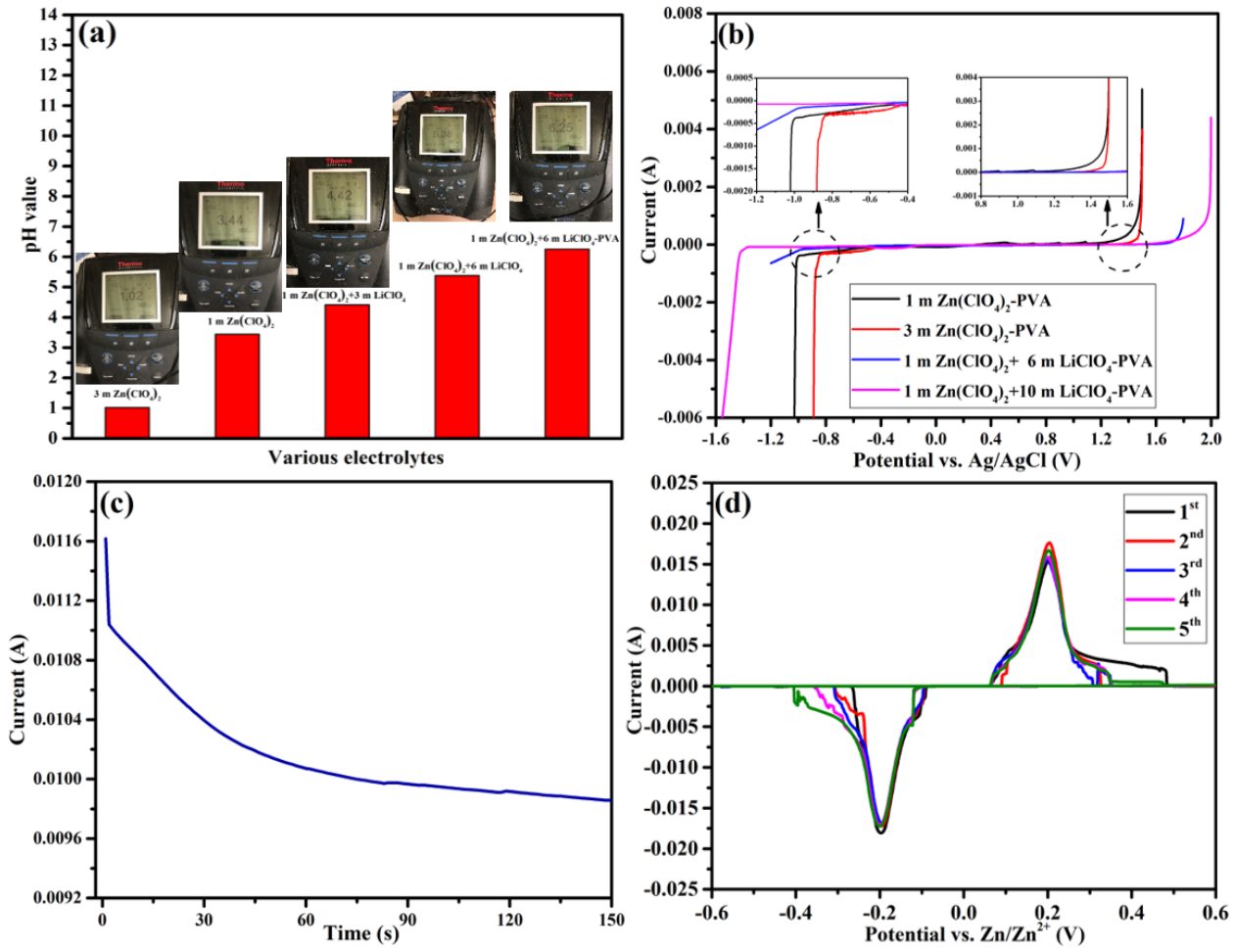

Figure 2. pH value of various electrolytes with optical images of pH meter as inset (a); Stability window test on four different electrolytes (1 m $Zn(ClO_4)_2$-PVA, 3 m $Zn(ClO_4)_2$-PVA, 1 m $Zn(ClO_4)_2$ + 6 m $LiClO_4$-PVA and 1 m $Zn(ClO_4)_2$+10 m $LiClO_4$-PVA) (b); The current interrupt test on Zn/Zn symmetric cell based on 1 m $Zn(ClO_4)_2$+10 m $LiClO_4$-PVA OSGE under 1.0 V vs. Zn/Zn^{2+} applied voltage (c); CV curves of Zn symmetric cell basing on the 1 m $Zn(ClO_4)_2$ + 10 m $LiClO_4$-PVA OSGE under 1 $mV \cdot s^{-1}$ scanning rate (d).

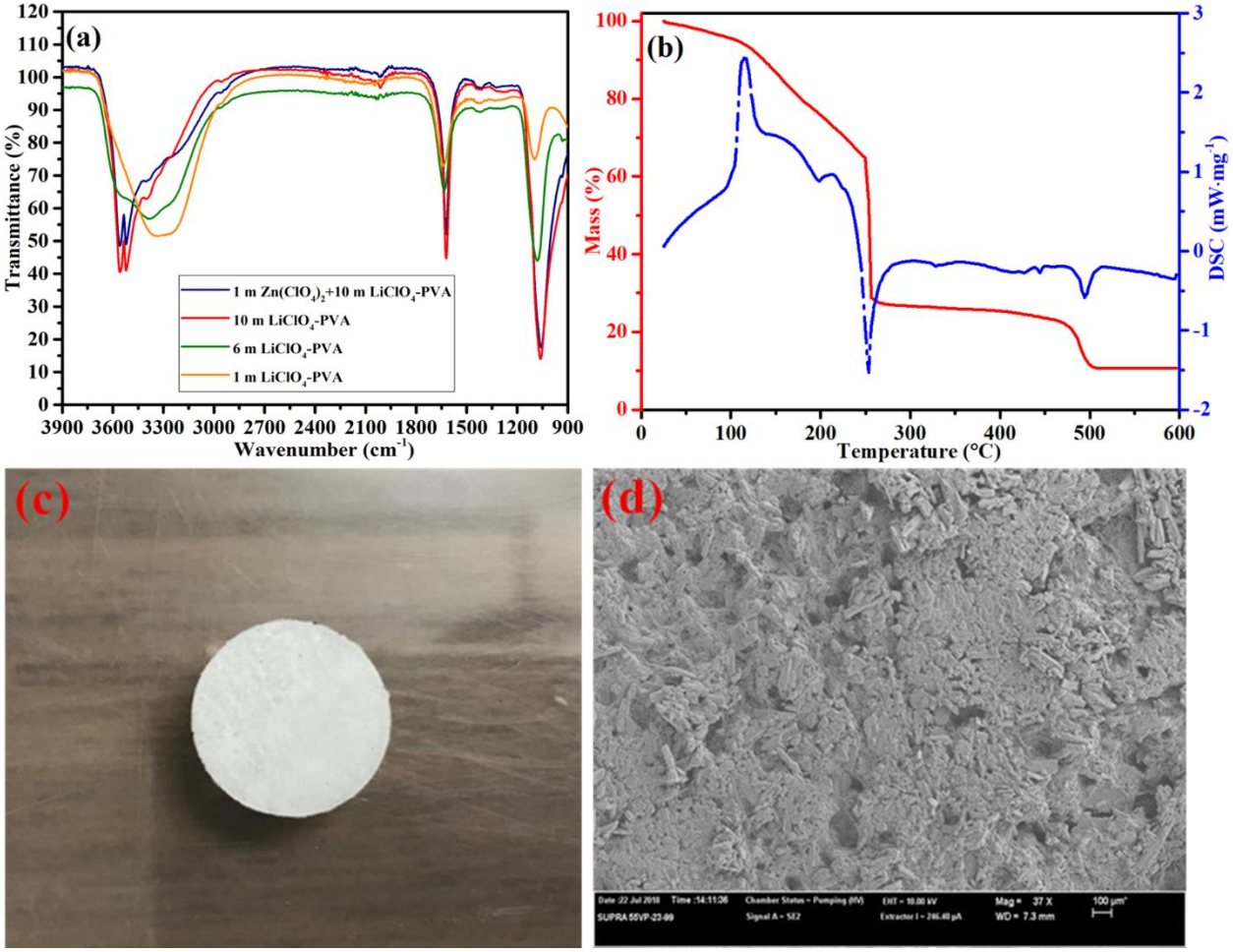

Figure 3. FTIR spectra of various electrolytes (a); TGA analysis on the 1 m $Zn(ClO_4)_2$+10 m $LiClO_4$-PVA electrolyte from room temperature to 600℃ (b); Optical image of 1 m $Zn(ClO_4)_2$+10 m $LiClO_4$-PVA electrolyte after tape casting on the glass microfiber filter (c); SEM image regarding surface of 1 m $Zn(ClO_4)_2$+10 m $LiClO_4$-PVA electrolyte with 37 X magnification (d).

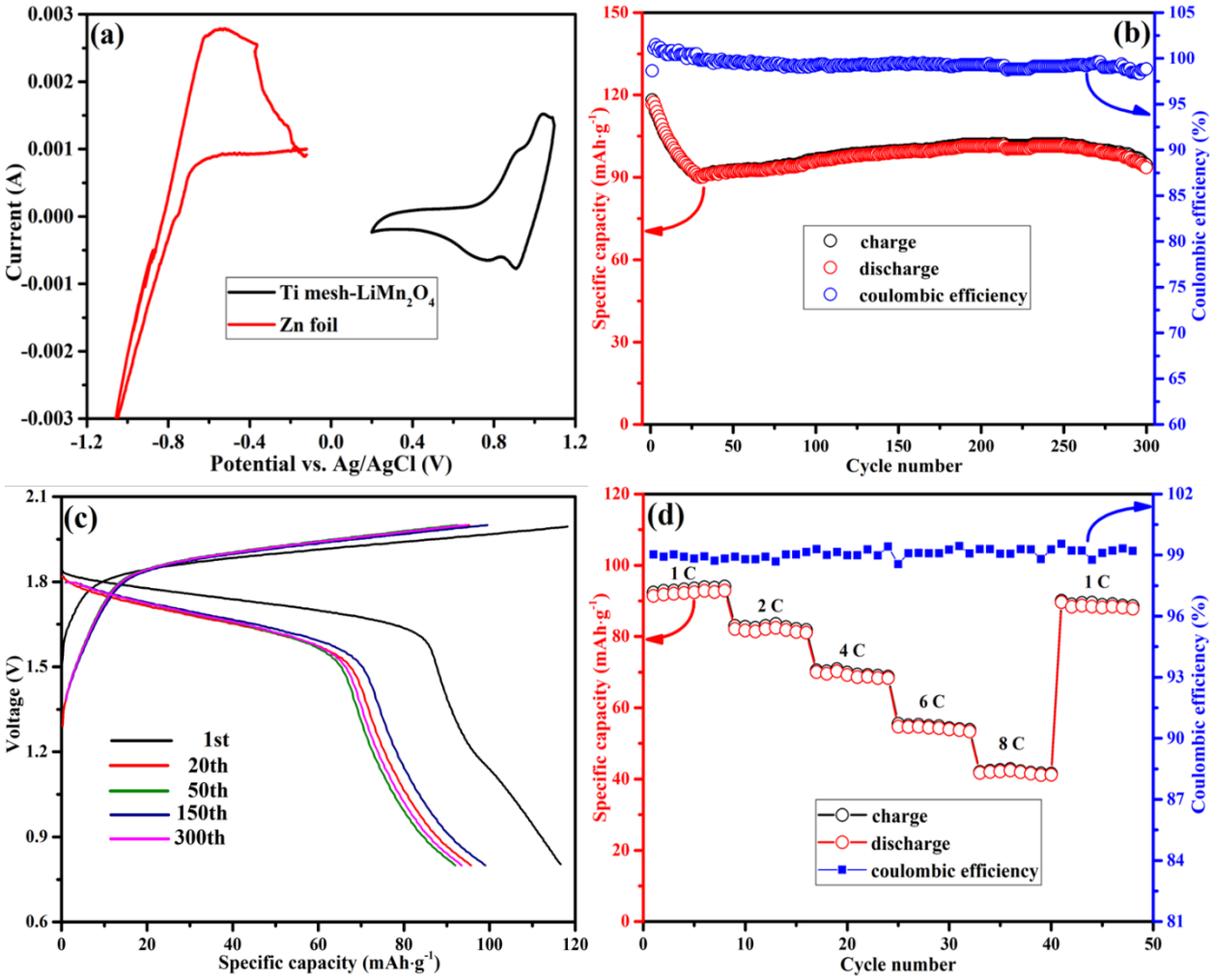

Figure 4. CV curves of Zn and Ti mesh-$LiMn_2O_4$ electrodes with Ti foil as counter electrode and Ag/AgCl as reference electrode (a); Cyclic performance of Zn/$LiMn_2O_4$ full cell under 1 C rate between 0.8 and 2.0 versus Zn/Zn^{2+} within 300 cycles (b); Accordingly charge-discharge curves of Zn/$LiMn_2O_4$ full cell between 0.8 and 2.0 V versus Zn/Zn^{2+} of 1^{st}, 20^{th}, 50^{th}, 150^{th} and 300^{th} cycles (c); Rate performance of Zn/$LiMn_2O_4$ full cell under 1, 2, 4, 6 and 8 C rate (d).

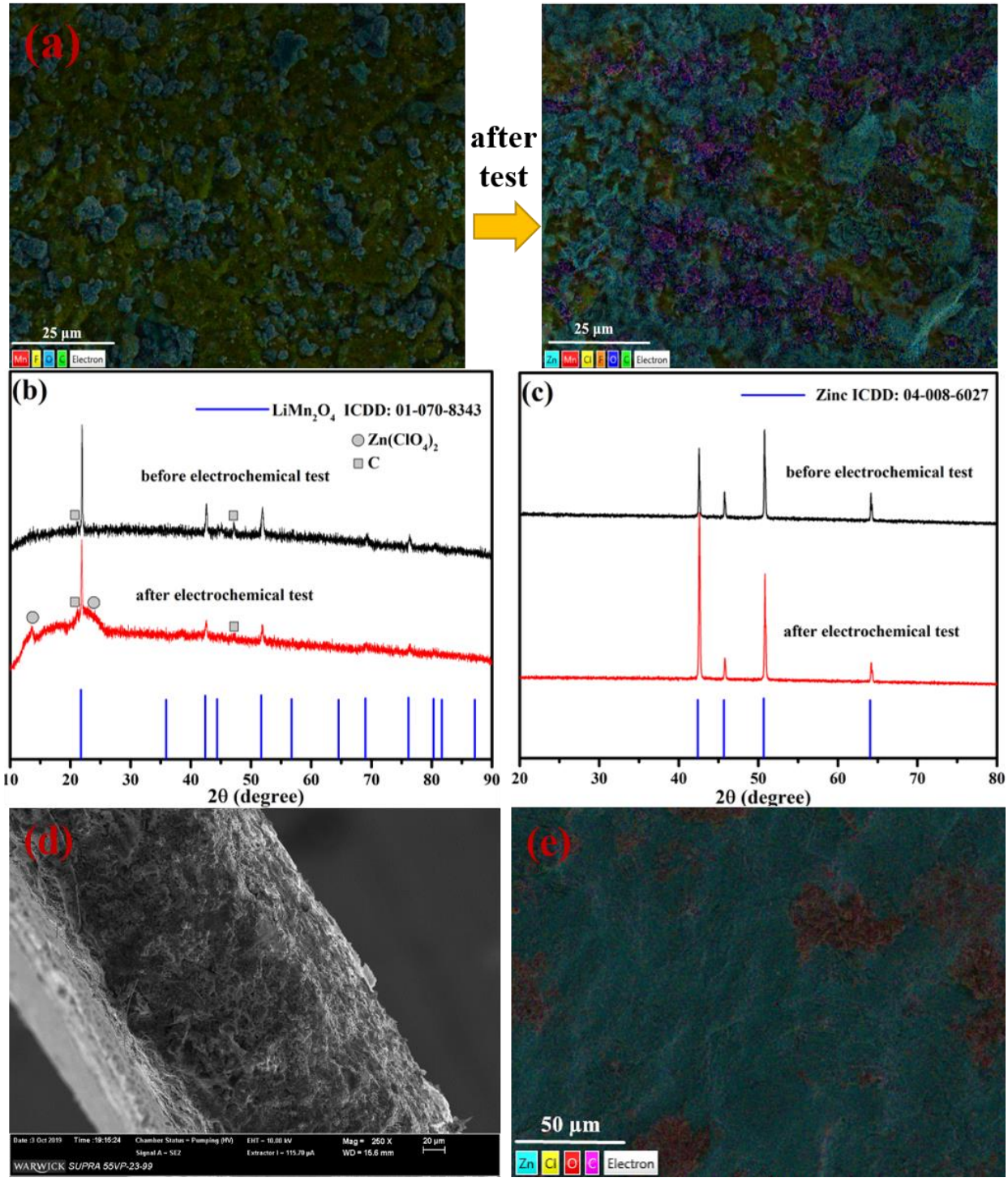

Fig. 5. EDX layered mapping of Ti mesh-$LiMn_2O_4$ electrode before and after electrochemical test (a); XRD patterns of Ti mesh-$LiMn_2O_4$ electrode before and after electrochemical test (b); XRD patterns of Zn foil electrode before and after electrochemical test (c); SEM image of cross-section

of Zn foil electrode after electrochemical test (d); Layered mapping of Zn foil electrode after electrochemical test (e).

ASSOCIATED CONTENT

Supporting Information

The Supporting Information is available free of charge at

https://pubs.acs.org/doi/10.1021/acsaem.xxxxxxx.

Stability window and ionic conductivity of different electrolytes at various temperatures; Stability window of 10 m $LiClO_4$ at different scanning rates; CV curves of Zn symmetric cells; EIS, XRD, SEM, FTIR and TGA of the materials. (PDF)

AUTHOR INFORMATION

Corresponding Author

*Email: S.Tao.1@warwick.ac.uk (S. T.).

Author Contributions

The manuscript was written through contributions of all authors. All authors have given approval to the final version of the manuscript.

ACKNOWLEDGMENT

One of the authors, S.G. Chen thanks China Scholarship Council (CSC) for a fully funded scholarship to support his PhD study at University of Warwick.

REFERENCES

1. Alias, N.; Mohamad, A. A., Advances of aqueous rechargeable lithium-ion battery: A review. *Journal of Power Sources* **2015,** *274*, 237-251.
2. Aurbach, D.; McCloskey, B. D.; Nazar, L. F.; Bruce, P. G., Advances in understanding mechanisms underpinning lithium–air batteries. *Nature Energy* **2016,** *1*, 16128.

3. Kim, H.; Hong, J.; Park, K.-Y.; Kim, H.; Kim, S.-W.; Kang, K., Aqueous rechargeable Li and Na ion batteries. *Chemical Reviews* **2014,** *114* (23), 11788-11827.
4. Manthiram, A.; Yu, X.; Wang, S., Lithium battery chemistries enabled by solid-state electrolytes. *Nature Reviews Materials* **2017,** *2*, 16103.
5. Tarascon, J. M., Key challenges in future Li-battery research. *Philosophical Transactions of the Royal Society A: Mathematical, Physical and Engineering Sciences* **2010,** *368* (1923), 3227-3241.
6. Wang, X.; Wang, F.; Wang, L.; Li, M.; Wang, Y.; Chen, B.; Zhu, Y.; Fu, L.; Zha, L.; Zhang, L.; Wu, Y.; Huang, W., An aqueous rechargeable Zn//Co_3O_4 battery with high energy density and good cycling behavior. *Adv. Mater.* **2016,** *28* (24), 4904-4911.
7. Chen, L.; Gu, Q.; Zhou, X.; Lee, S.; Xia, Y.; Liu, Z., New-concept batteries based on aqueous Li^+/Na^+ mixed-ion electrolytes. *Scientific Reports* **2013,** *3*, 1946.
8. Kundu, D.; Adams, B. D.; Duffort, V.; Vajargah, S. H.; Nazar, L. F., A high-capacity and long-life aqueous rechargeable zinc battery using a metal oxide intercalation cathode. *Nature Energy* **2016,** *1*, 16119.
9. Zeng, X. H.; Hao, J. N.; Wang, Z. J.; Mao, J. F.; Guo, Z. P., Recent progress and perspectives on aqueous Zn-based rechargeable batteries with mild aqueous electrolytes. *Energy Storage Materials* **2019,** *20*, 410-437.
10. Ma, L. T.; Li, N.; Long, C. B.; Dong, B. B.; Fang, D. L.; Liu, Z. X.; Zhao, Y. W.; Li, X. L.; Fan, J.; Chen, S. M.; Zhang, S. J.; Zhi, C. Y., Achieving Both High Voltage and High Capacity in Aqueous Zinc-Ion Battery for Record High Energy Density. *Advanced Functional Materials* **2019**.
11. Wan, F.; Zhang, L.; Dai, X.; Wang, X.; Niu, Z.; Chen, J., Aqueous rechargeable zinc/sodium vanadate batteries with enhanced performance from simultaneous insertion of dual carriers. *Nature Communications* **2018,** *9* (1), 1656.
12. Liu, C.; Wang, X.; Deng, W.; Li, C.; Chen, J.; Xue, M.; Li, R.; Pan, F., Engineering Fast Ion Conduction and Selective Cation Channels for a High-Rate and High-Voltage Hybrid Aqueous Battery. *Angewandte Chemie International Edition* **2018,** *57* (24), 7046-7050.
13. Wu, X.; Xiang, Y.; Peng, Q.; Wu, X.; Li, Y.; Tang, F.; Song, R.; Liu, Z.; He, Z.; Wu, X., Green-low-cost rechargeable aqueous zinc-ion batteries using hollow porous spinel ZnMn2O4 as the cathode material. *Journal of Materials Chemistry A* **2017,** *5* (34), 17990-17997.
14. He, P.; Yan, M.; Zhang, G.; Sun, R.; Chen, L.; An, Q.; Mai, L., Layered VS_2 nanosheet-based aqueous Zn Ion battery cathode. *Advanced Energy Materials* **2017,** *7* (11), 1601920.
15. Huang, J.; Wang, Z.; Hou, M.; Dong, X.; Liu, Y.; Wang, Y.; Xia, Y., Polyaniline-intercalated manganese dioxide nanolayers as a high-performance cathode material for an aqueous zinc-ion battery. *Nature Communications* **2018,** *9* (1), 2906.
16. Tan, P.; Chen, B.; Xu, H.; Zhang, H.; Cai, W.; Ni, M.; Liu, M.; Shao, Z., Flexible Zn– and Li–air batteries: recent advances, challenges, and future perspectives. *Energy & Environmental Science* **2017,** *10* (10), 2056-2080.
17. Liu, Z.; Li, H.; Zhu, M.; Huang, Y.; Tang, Z.; Pei, Z.; Wang, Z.; Shi, Z.; Liu, J.; Huang, Y.; Zhi, C., Towards wearable electronic devices: A quasi-solid-state aqueous lithium-ion battery with outstanding stability, flexibility, safety and breathability. *Nano Energy* **2018,** *44*, 164-173.

18. Zeng, Y.; Zhang, X.; Meng, Y.; Yu, M.; Yi, J.; Wu, Y.; Lu, X.; Tong, Y., Achieving ultrahigh energy density and long durability in a flexible rechargeable quasi-solid-state Zn–MnO_2 battery. *Adv. Mater.* **2017,** *29* (26), 1700274.
19. Yamada, Y.; Wang, J.; Ko, S.; Watanabe, E.; Yamada, A., Advances and issues in developing salt-concentrated battery electrolytes. *Nature Energy* **2019,** *4* (4), 269-280.
20. Yamada, Y.; Usui, K.; Sodeyama, K.; Ko, S.; Tateyama, Y.; Yamada, A., Hydrate-melt electrolytes for high-energy-density aqueous batteries. *Nature Energy* **2016,** *1* (10), 16129.
21. Suo, L.; Borodin, O.; Gao, T.; Olguin, M.; Ho, J.; Fan, X.; Luo, C.; Wang, C.; Xu, K., "Water-in-salt" electrolyte enables high-voltage aqueous lithium-ion chemistries. *Science* **2015,** *350* (6263), 938-943.
22. Suo, L.; Borodin, O.; Sun, W.; Fan, X.; Yang, C.; Wang, F.; Gao, T.; Ma, Z.; Schroeder, M.; von Cresce, A.; Russell, S. M.; Armand, M.; Angell, A.; Xu, K.; Wang, C., Advanced high-voltage aqueous lithium-ion battery enabled by "water-in-bisalt" electrolyte. *Angewandte Chemie International Edition* **2016,** *55* (25), 7136-7141.
23. Yang, C.; Chen, J.; Ji, X.; Pollard, T. P.; Lü, X.; Sun, C.-J.; Hou, S.; Liu, Q.; Liu, C.; Qing, T.; Wang, Y.; Borodin, O.; Ren, Y.; Xu, K.; Wang, C., Aqueous Li-ion battery enabled by halogen conversion–intercalation chemistry in graphite. *Nature* **2019,** *569* (7755), 245-250.
24. Zheng, J. X.; Tan, G. Y.; Shan, P.; Liu, T. C.; Hu, J. T.; Feng, Y. C.; Yang, L. Y.; Zhang, M. J.; Chen, Z. H.; Lin, Y.; Lu, J.; Neuefeind, J. C.; Ren, Y.; Amine, K.; Wang, L. W.; Xu, K.; Pan, F., Understanding Thermodynamic and Kinetic Contributions in Expanding the Stability Window of Aqueous Electrolytes. *Chem* **2018,** *4* (12), 2872-2882.
25. Leonard, D. P.; Wei, Z.; Chen, G.; Du, F.; Ji, X., Water-in-salt electrolyte for potassium-ion batteries. *ACS Energy Letters* **2018,** *3* (2), 373-374.
26. Lukatskaya, M. R.; Feldblyum, J. I.; Mackanic, D. G.; Lissel, F.; Michels, D. L.; Cui, Y.; Bao, Z., Concentrated mixed cation acetate "water-in-salt" solutions as green and low-cost high voltage electrolytes for aqueous batteries. *Energy & Environmental Science* **2018,** *11* (10), 2876-2883.
27. Younesi, R.; Veith, G. M.; Johansson, P.; Edström, K.; Vegge, T., Lithium salts for advanced lithium batteries: Li–metal, Li–O_2, and Li–S. *Energy & Environmental Science* **2015,** *8* (7), 1905-1922.
28. Li, W.; Dahn, J. R.; Wainwright, D. S., Rechargeable Lithium Batteries with Aqueous Electrolytes. *Science* **1994,** *264* (5162), 1115-1118.
29. Wang, F.; Borodin, O.; Gao, T.; Fan, X.; Sun, W.; Han, F.; Faraone, A.; Dura, J. A.; Xu, K.; Wang, C., Highly reversible zinc metal anode for aqueous batteries. *Nature Materials* **2018,** *17* (6), 543-549.
30. Wei, J.; Wei, G.; Shang, Y.; Zhou, J.; Wu, C.; Wang, Q., Dissolution–Crystallization Transition within a Polymer Hydrogel for a Processable Ultratough Electrolyte. *Adv. Mater.* **2019,** *31* (30), 1900248.
31. Wang, G.; Lu, X.; Ling, Y.; Zhai, T.; Wang, H.; Tong, Y.; Li, Y., LiCl/PVA Gel Electrolyte Stabilizes Vanadium Oxide Nanowire Electrodes for Pseudocapacitors. *ACS Nano* **2012,** *6* (11), 10296-10302.
32. Yang, C. Y.; Ji, X.; Fan, X. L.; Gao, T.; Suo, L. M.; Wang, F.; Sun, W.; Chen, J.; Chen, L.; Han, F. D.; Miao, L.; Xu, K.; Gerasopoulos, K.; Wang, C. S., Flexible Aqueous Li-Ion Battery with High Energy and Power Densities. *Adv. Mater.* **2017,** *29* (44).

33. Lan, R.; Tao, S. W.; Irvine, J. T. S., A direct urea fuel cell - power from fertiliser and waste. *Energy & Environmental Science* **2010,** *3* (4), 438-441.
34. Yan, J.; Wang, J.; Liu, H.; Bakenov, Z.; Gosselink, D.; Chen, P., Rechargeable hybrid aqueous batteries. *Journal of Power Sources* **2012,** *216*, 222-226.
35. Li, C. Y.; Zhang, D. X.; Ma, F. X.; Ma, T. Y.; Wang, J.; Chen, Y. H.; Zhu, Y. S.; Fu, L. J.; Wu, Y. P.; Huang, W., A High-Rate and Long-Life Aqueous Rechargeable Ammonium Zinc Hybrid Battery. *Chemsuschem* **2019,** *12* (16), 3732-3736.
36. Li, H. Z.; Firby, C. J.; Elezzabi, A. Y., Rechargeable Aqueous Hybrid Zn2+/Al3+ Electrochromic Batteries. *Joule* **2019,** *3* (9), 2268-2278.
37. Ao, H. S.; Zhao, Y. Y.; Zhou, J.; Cai, W. L.; Zhang, X. T.; Zhu, Y. C.; Qian, Y. T., Rechargeable aqueous hybrid ion batteries: developments and prospects. *Journal of Materials Chemistry A* **2019,** *7* (32), 18708-18734.
38. Hoang, T. K. A.; Doan, T. N. L.; Lu, C. Y.; Ghaznavi, M.; Zhao, H. B.; Chen, P., Performance of Thixotropic Gel Electrolytes in the Rechargeable Aqueous Zn/LiMn2O4 Battery. *Acs Sustainable Chemistry & Engineering* **2017,** *5* (2), 1804-1811.
39. Xiong, W. L.; Yang, D. J.; Hoang, T. K. A.; Ahmed, M.; Zhi, J.; Qiu, X. Q.; Chen, P., Controlling the sustainability and shape change of the zinc anode in rechargeable aqueous Zn/LiMn2O4 battery. *Energy Storage Materials* **2018,** *15*, 131-138.
40. Xiong, W. L.; Hoang, T. K. A.; Yang, D. J.; Liu, Y.; Ahmed, M.; Xu, J. L.; Qiu, X. Q.; Chen, P., Electrolyte engineering for a highly stable, rechargeable hybrid aqueous battery. *Journal of Energy Storage* **2019,** *26*.
41. Xu, C.; Li, B.; Du, H.; Kang, F., Energetic Zinc Ion Chemistry: The Rechargeable Zinc Ion Battery. *Angewandte Chemie International Edition* **2012,** *51* (4), 933-935.
42. Zhou, L.; Zhao, D.; Lou, X., LiNi0.5Mn1.5O4 Hollow Structures as High-Performance Cathodes for Lithium-Ion Batteries. *Angewandte Chemie International Edition* **2012,** *51* (1), 239-241.
43. Hoang, T. K. A.; Acton, M.; Chen, H. T. H.; Huang, Y.; Doan, T. N. L.; Chen, P., Sustainable gel electrolyte containing Pb^{2+} as corrosion inhibitor and dendrite suppressor for the zinc anode in the rechargeable hybrid aqueous battery. *Materials Today Energy* **2017,** *4*, 34-40.
44. Veith, G. M.; Nanda, J.; Delmau, L. H.; Dudney, N. J., Influence of lithium salts on the discharge chemistry of Li–air cells. *The Journal of Physical Chemistry Letters* **2012,** *3* (10), 1242-1247.
45. Younesi, R.; Hahlin, M.; Edström, K., Surface characterization of the carbon cathode and the lithium anode of Li–O_2 batteries using $LiClO_4$ or LiBOB salts. *ACS Applied Materials & Interfaces* **2013,** *5* (4), 1333-1341.
46. Xu, K.; Ding, S. P.; Jow, T. R., Toward Reliable Values of Electrochemical Stability Limits for Electrolytes. *Journal of The Electrochemical Society* **1999,** *146* (11), 4172-4178.
47. Pratt, K. W.; Koch, W. F.; Wu, Y. C.; Berezansky, P. A., Molality-based primary standards of electrolytic conductivity (IUPAC Technical Report). In *Pure and Applied Chemistry*, 2001; Vol. 73, p 1783.
48. Nagarale, R. K.; Shahi, V. K.; Rangarajan, R., Preparation of polyvinyl alcohol–silica hybrid heterogeneous anion-exchange membranes by sol–gel method and their characterization. *Journal of Membrane Science* **2005,** *248* (1), 37-44.
49. Fergus, J. W., Ceramic and polymeric solid electrolytes for lithium-ion batteries. *Journal of Power Sources* **2010,** *195* (15), 4554-4569.

50. Luo, J.-Y.; Cui, W.-J.; He, P.; Xia, Y.-Y., Raising the cycling stability of aqueous lithium-ion batteries by eliminating oxygen in the electrolyte. *Nature Chemistry* **2010,** *2*, 760.
51. Liao, H.; Liu, Y.; Wang, Q.; Duan, W., Structure and properties of porous poly(vinyl alcohol) hydrogel beads prepared through a physical–chemical crosslinking method. *Applied polymer scinece* **2018,** *135* (26), 46402.
52. Chen, Y.; Zhang, Y.-H.; Zhao, L.-J., ATR-FTIR spectroscopic studies on aqueous $LiClO_4$, $NaClO_4$, and $Mg(ClO_4)_2$ solutions. *Physical Chemistry Chemical Physics* **2004,** *6* (3), 537-542.
53. Zheng, J.; Tan, G.; Shan, P.; Liu, T.; Hu, J.; Feng, Y.; Yang, L.; Zhang, M.; Chen, Z.; Lin, Y.; Lu, J.; Neuefeind, J. C.; Ren, Y.; Amine, K.; Wang, L.-W.; Xu, K.; Pan, F., Understanding Thermodynamic and Kinetic Contributions in Expanding the Stability Window of Aqueous Electrolytes. *Chem* **2018,** *4* (12), 2872-2882.
54. Sheela, T.; Bhajantri, R. F.; Nambissan, P. M. G.; Ravindrachary, V.; Lobo, B.; Naik, J.; Rathod, S. G., Ionic conductivity and free volume related microstructural properties of $LiClO_4$/PVA/NaAlg polymer composites: Positron annihilation spectroscopic studies. *Journal of Non-Crystalline Solids* **2016,** *454*, 19-30.
55. Gordon, S.; Campbell, C., Differential thermal analysis of inorganic compounds. *Analytical Chemistry* **1955,** *27* (7), 1102-1109.
56. Luo, J.-Y.; Xia, Y.-Y., Aqueous Lithium-ion Battery LiTi2(PO4)3/LiMn2O4 with High Power and Energy Densities as well as Superior Cycling Stability**. *Advanced Functional Materials* **2007,** *17* (18), 3877-3884.
57. Sun, W.; Wang, F.; Hou, S.; Yang, C.; Fan, X.; Ma, Z.; Gao, T.; Han, F.; Hu, R.; Zhu, M.; Wang, C., Zn/MnO_2 battery chemistry with H^+ and Zn^{2+} coinsertion. *Journal of the American Chemical Society* **2017,** *139* (29), 9775-9778.
58. Hoang, T. K. A.; Doan, T. N. L.; Cho, J. H.; Su, J. Y. J.; Lee, C.; Lu, C.; Chen, P., Sustainable Gel Electrolyte Containing Pyrazole as Corrosion Inhibitor and Dendrite Suppressor for Aqueous Zn/LiMn2O4 Battery. *ChemSusChem* **2017,** *10* (13), 2816-2822.
59. Hoang, T. K. A.; Doan, T. N. L.; Lu, C.; Ghaznavi, M.; Zhao, H.; Chen, P., Performance of Thixotropic Gel Electrolytes in the Rechargeable Aqueous Zn/LiMn2O4 Battery. *ACS Sustainable Chemistry & Engineering* **2017,** *5* (2), 1804-1811.
60. Xiong, W.; Yang, D.; Hoang, T. K. A.; Ahmed, M.; Zhi, J.; Qiu, X.; Chen, P., Controlling the sustainability and shape change of the zinc anode in rechargeable aqueous Zn/LiMn2O4 battery. *Energy Storage Materials* **2018,** *15*, 131-138.
61. Chung, K. Y.; Lee, H. S.; Yoon, W.-S.; McBreen, J.; Yang, X.-Q., Studies of LiMn2O4 Capacity Fading at Elevated Temperature Using In Situ Synchrotron X-Ray Diffraction. *Journal of The Electrochemical Society* **2006,** *153* (4), A774-A780.
62. Silva, V. B.; Rouboa, A., Hydrogen-fed PEMFC: overvoltage analysis during an activation procedure. *Journal of Electroanalytical Chemistry* **2012,** *671*, 58-66.
63. Haanappel, V.; Mai, A.; Mertens, J., Electrode activation of anode-supported SOFCs with LSM-or LSCF-type cathodes. *Solid State Ionics* **2006,** *177* (19-25), 2033-2037.
64. Lin, D.; Liu, Y.; Cui, Y., Reviving the lithium metal anode for high-energy batteries. *Nature Nanotechnology* **2017,** *12*, 194-206.

Supporting Information

Perchlorate Based 'Oversaturated Gel Electrolyte' for Aqueous Rechargeable Hybrid Zn-Li Battery

Shigang Chen,[†] *Rong Lan,*[†] *John Humphreys,*[†] *and Shanwen Tao**[†,‡]

[†]School of Engineering, University of Warwick, Coventry CV4 7AL, UK.

[‡]Department of Chemical Engineering, Monash University, Clayton, Victoria 3800.

Keywords over-saturated gel, wide electrochemical window, quasi-solid-state, aqueous hybrid battery, zinc metal anode

Table S1. Summary of properties (stability window and ionic conductivity) of different electrolytes at various temperatures.

Electrolytes	Stability potential (vs. Ag/AgCl) at 1 $mV \cdot s^{-1}$ (V)	Electrochemical stability window (V)	Ionic conductivity ($S \cdot cm^{-1}$)
1 m $LiClO_4$-PVA at RT	-0.60 to 1.70	2.3	4.31×10^{-2}
6 m $LiClO_4$-PVA at RT	-0.90 to 1.70	2.6	9.9×10^{-2}
10 m $LiClO_4$-PVA at RT	-1.40 to 1.90	3.3	1.32×10^{-2}
10 m $LiClO_4$ at RT	-1.0 to 1.90	2.9	9.90×10^{-3}
1 m $Zn(ClO_4)_2$-PVA at RT	-1.0 to 1.10	2.1	7.27×10^{-3}
3 m $Zn(ClO_4)_2$-PVA at RT	-0.8 to 1.40	2.2	1.09×10^{-2}
1 m $Zn(ClO_4)_2$+6 m $LiClO_4$-PVA at RT	-1.0 to 1.60	2.6	2.20×10^{-2}
1 m $Zn(ClO_4)_2$+10 m $LiClO_4$-PVA at RT	-1.30 to 1.70	3.0	8.51×10^{-3}
10 m $LiClO_4$-PVA at 40℃	-1.30 to 1.70	3.0	1.05×10^{-1}
10 m $LiClO_4$-PVA at 60℃	-1.20 to 1.60	2.8	1.34×10^{-1}
10 m $LiClO_4$-PVA at 80℃	-1.00 to 1.50	2.5	1.86×10^{-1}

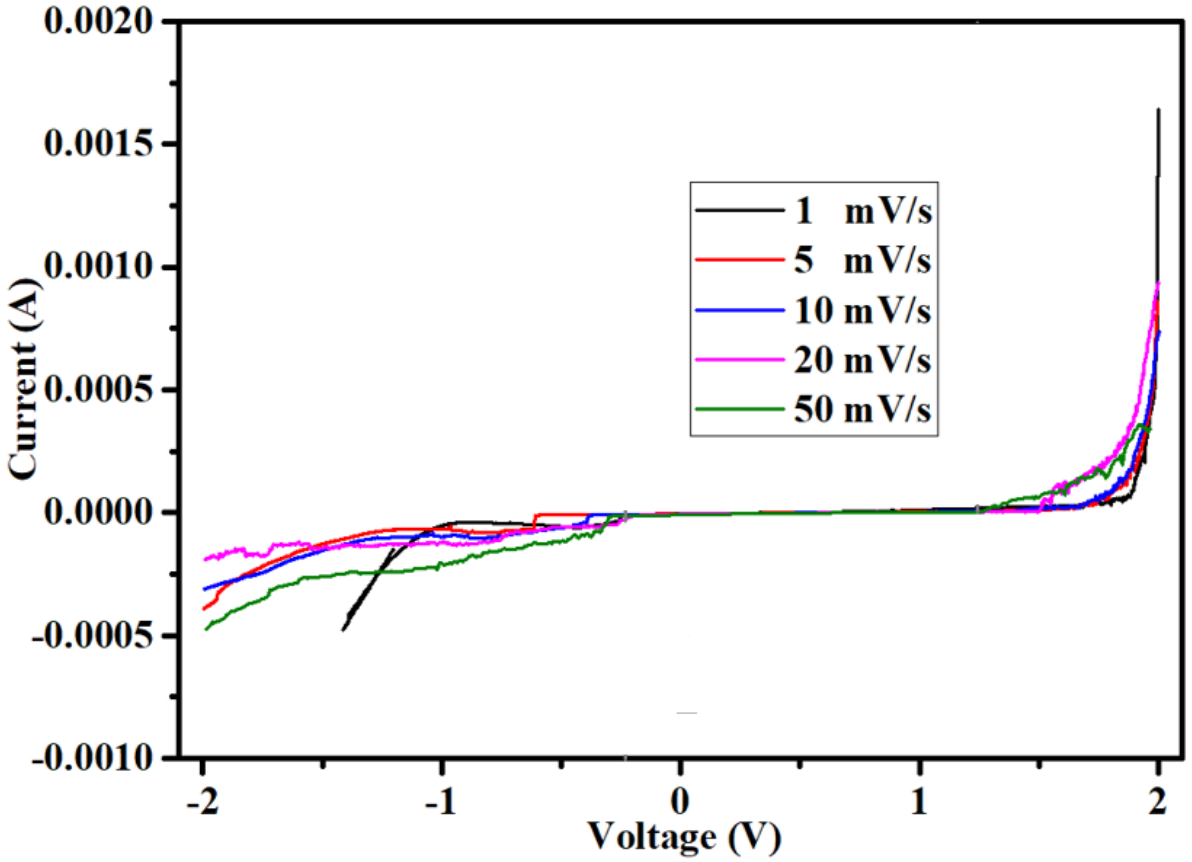

Figure S1. Stability window test on 10 m $LiClO_4$ over-saturated aqueous solution under scanning rates ranging from 50, 20, 10, 5 to 1 $mV \cdot s^{-1}$.

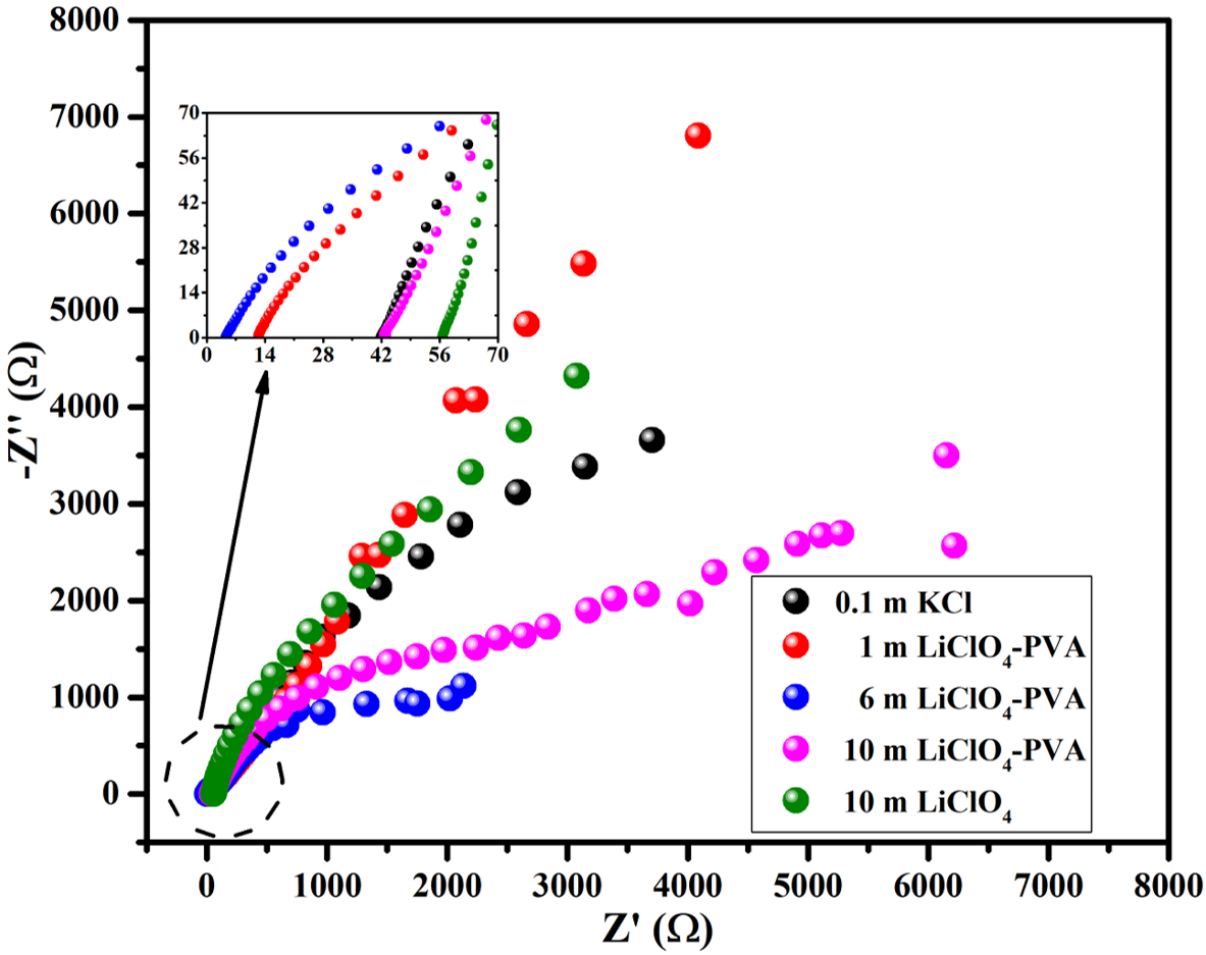

Figure S2. EIS patterns of 1, 6 and 10 m $LiClO_4$ with or without PVA electrolytes at room temperature.

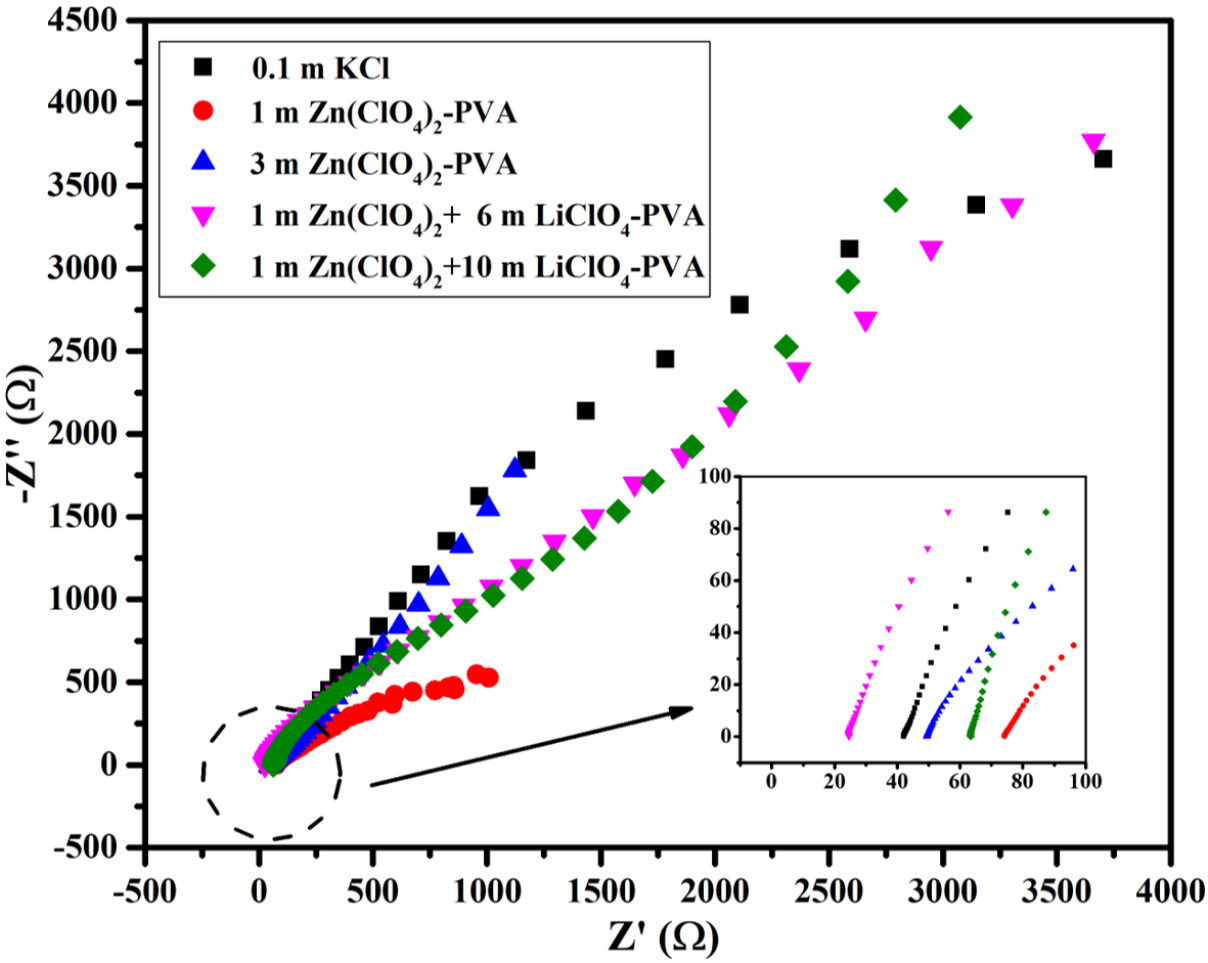

Figure S3. EIS patterns of 1 m $Zn(ClO_4)_2$-PVA, 3 m $Zn(ClO_4)_2$-PVA, 1 m $Zn(ClO_4)_2$+6 m $LiClO_4$-PVA and 1 m $Zn(ClO_4)_2$+10 m $LiClO_4$-PVA at room temperature.

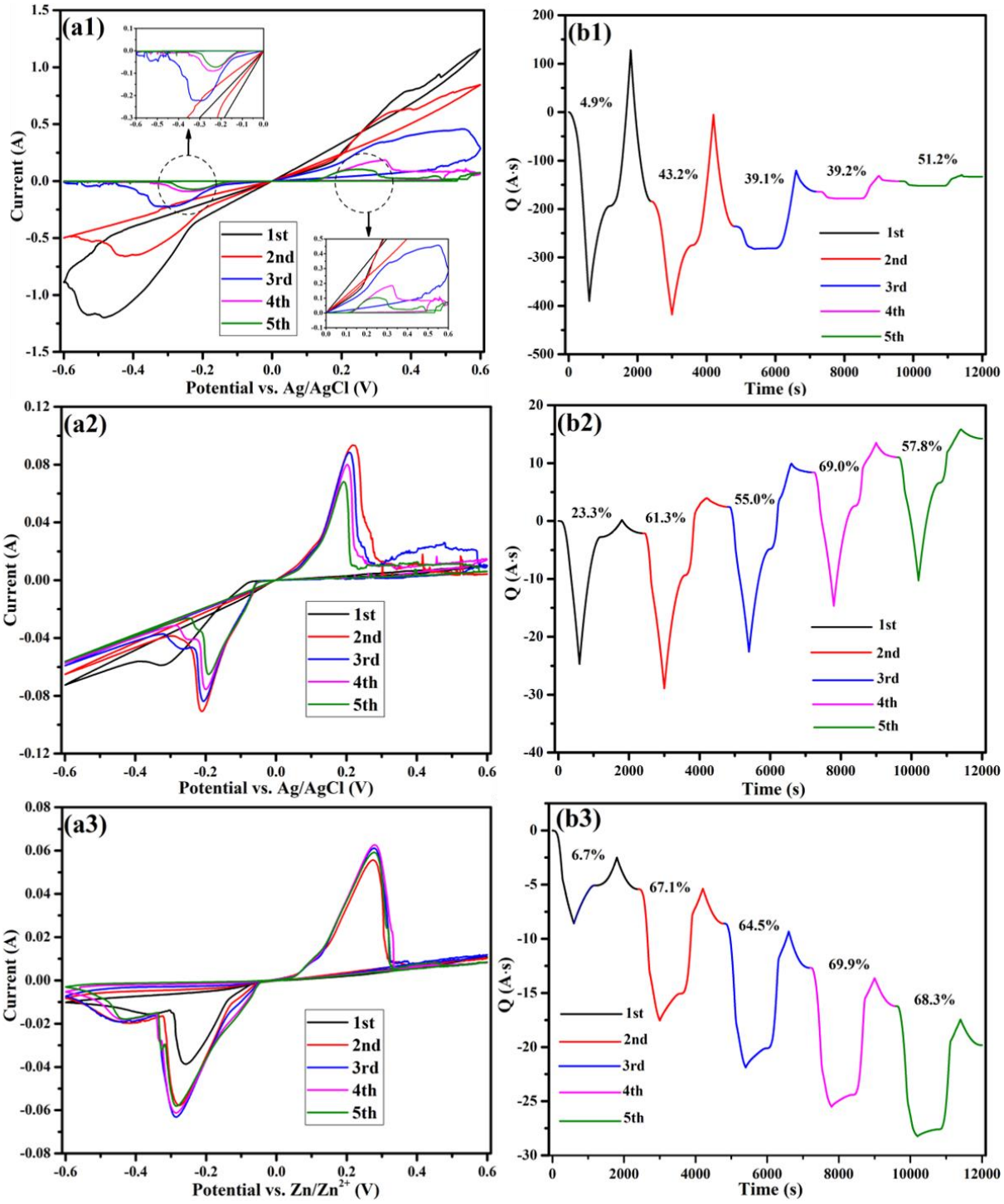

Figure S4. (a1-a3) CV curves of Zn symmetric cell based on the 1m $Zn(ClO_4)_2$-PVA, 3 m $Zn(ClO_4)_2$-PVA and 1 m $Zn(ClO_4)_2$ + 6 m $LiClO_4$-PVA electrolytes under 1 $mV \cdot s^{-1}$ scanning rate. (b1-b3) Corresponding chronocoulometry curves derived from the CV curves.

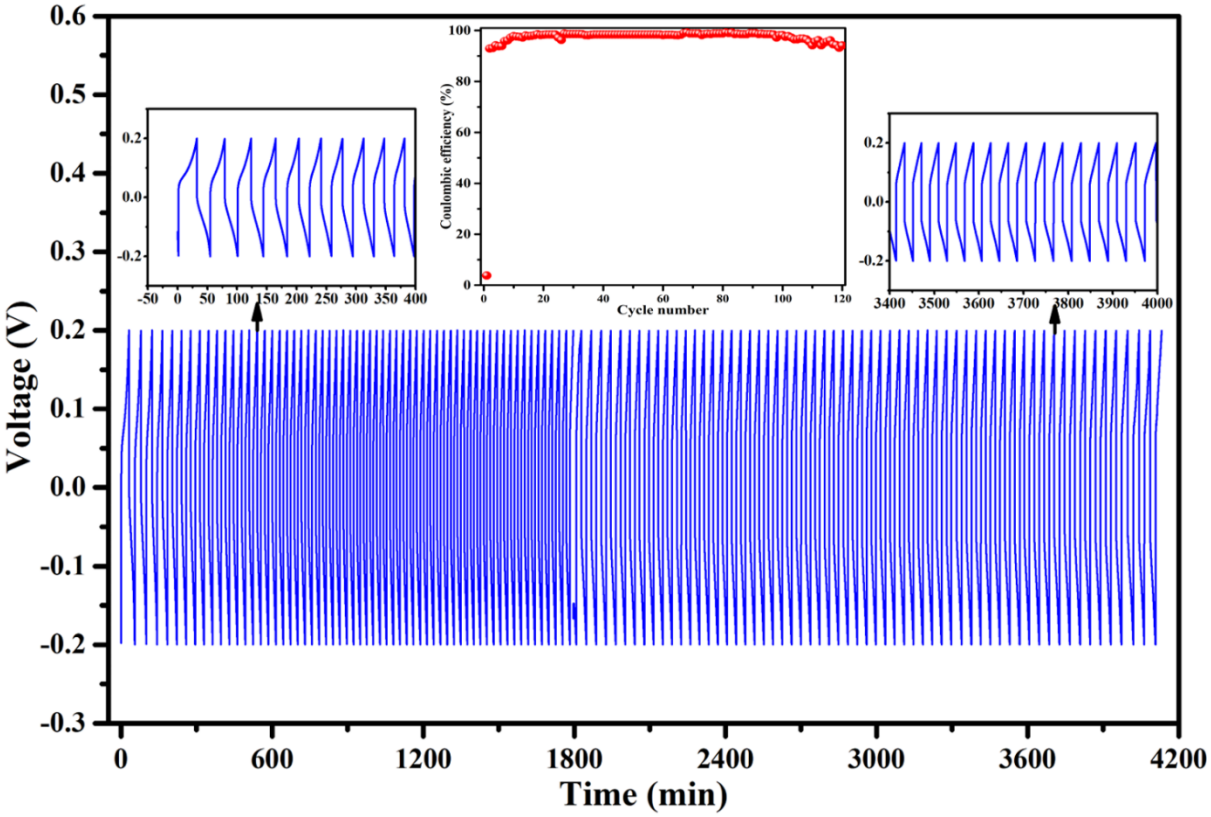

Figure S5. Cycling performance of Zn symmetric cell based on the 1m $Zn(ClO_4)_2$+10 m $LiClO_4$-PVA OSGE within the voltage range from -0.2 to 0.2 V under 5.0 mA·cm^{-2} current density.

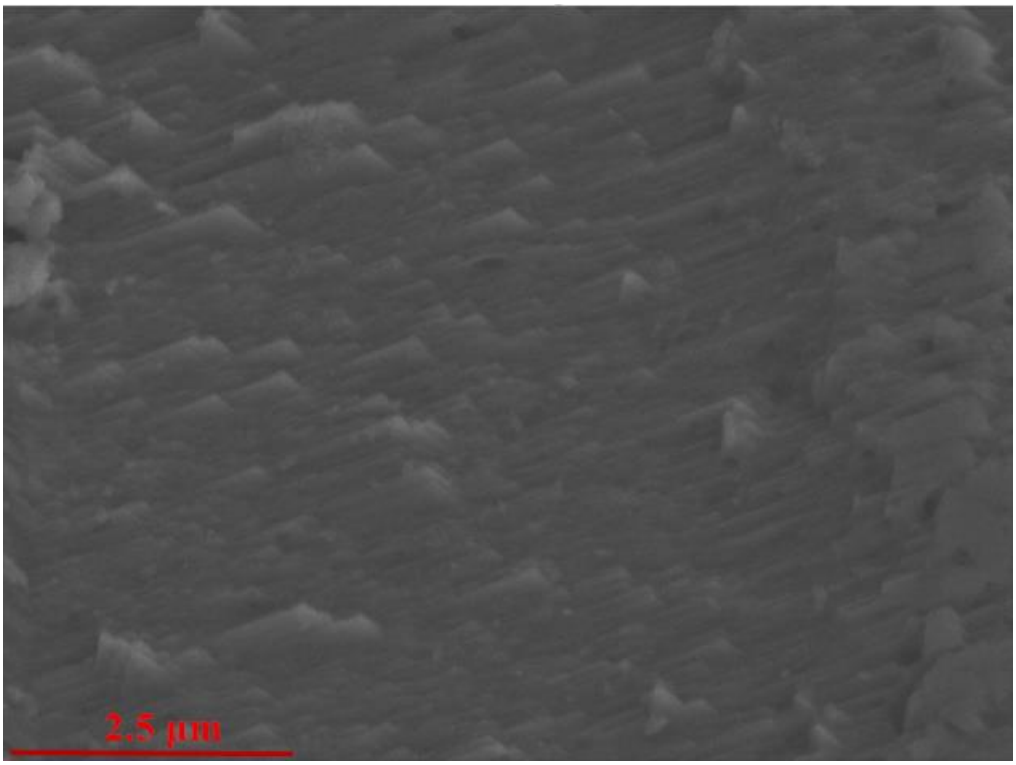

Figure S6. SEM image of Zn foil from the Zn symmetric cell after cyclic test with 2.5 µm resolution.

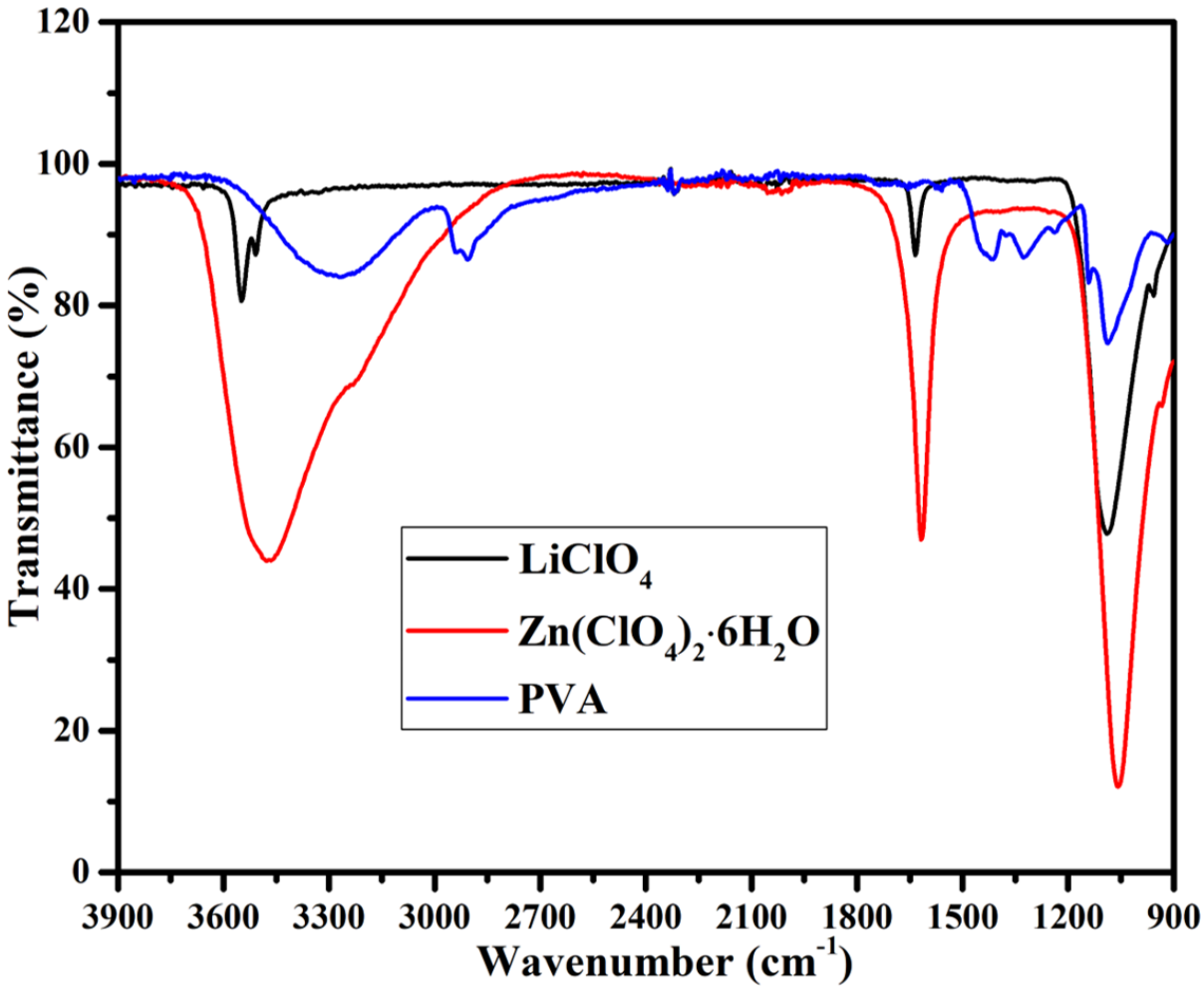

Figure S7. FTIR spectra of original chemicals serving as reference

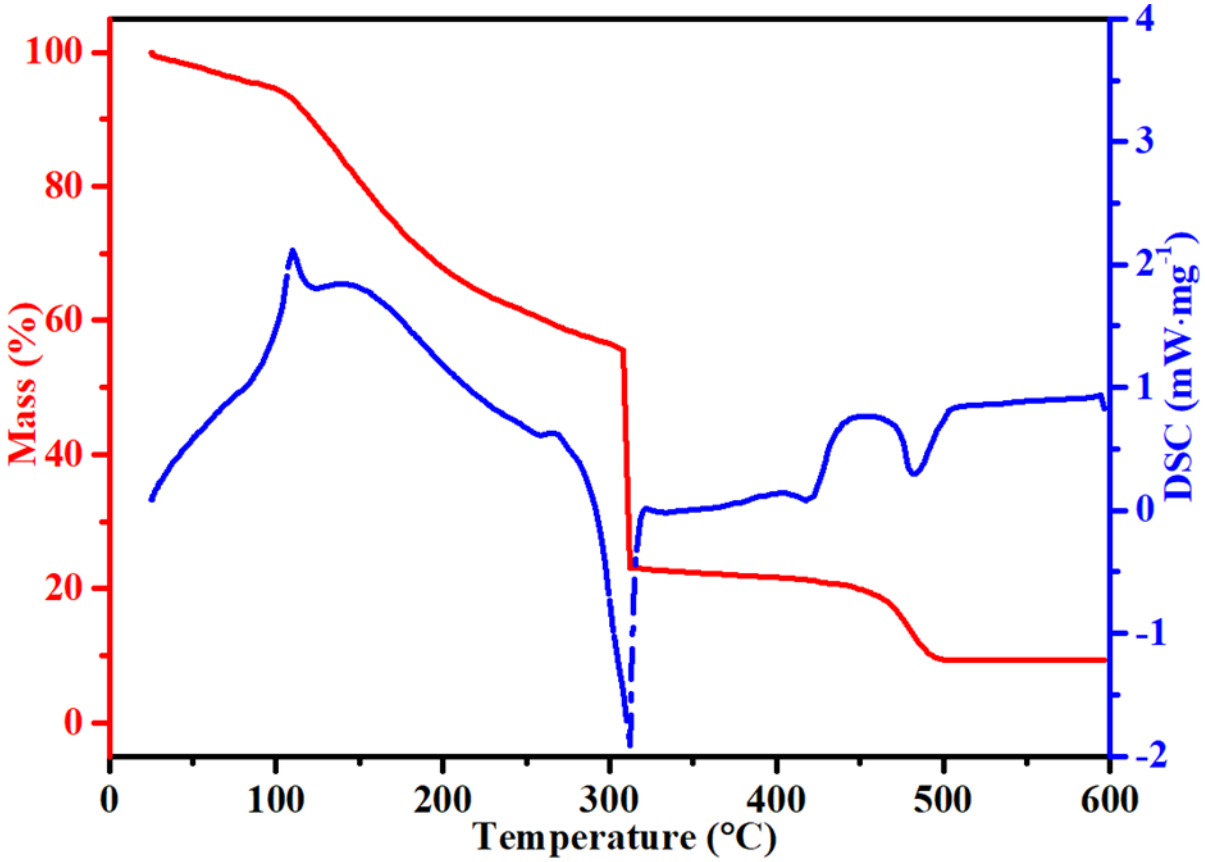
100
80
60
40
20
0
Mass (%)
4
3
2
1
0
-1
-2
DSC (mW·mg-1)
0
100
200
300
400
500
600
Temperature (°C)

Figure S8. TGA test on the 10 m $LiClO_4$-PVA electrolyte from room temperature to 600℃.

Figure S9. Optical image of top side of 1m $Zn(ClO_4)_2$+10 m $LiClO_4$-PVA OSGE at 95 □C before tape casting.

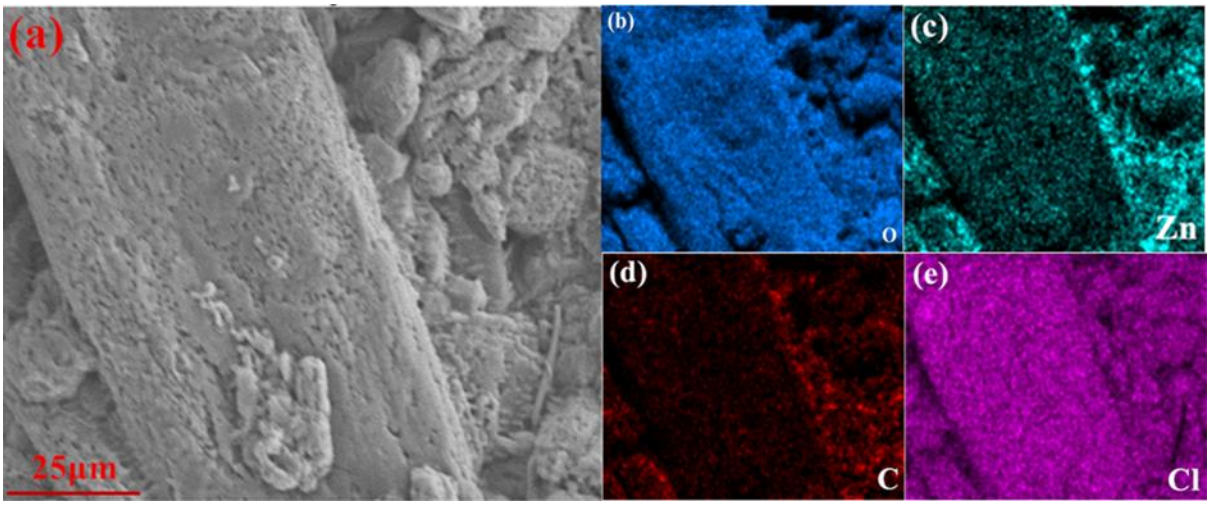

Figure S10. (a) SEM image of electrolyte with 25 μm resolution. (b, c, d, e) corresponding mapping of O, Zn, C and Cl element.

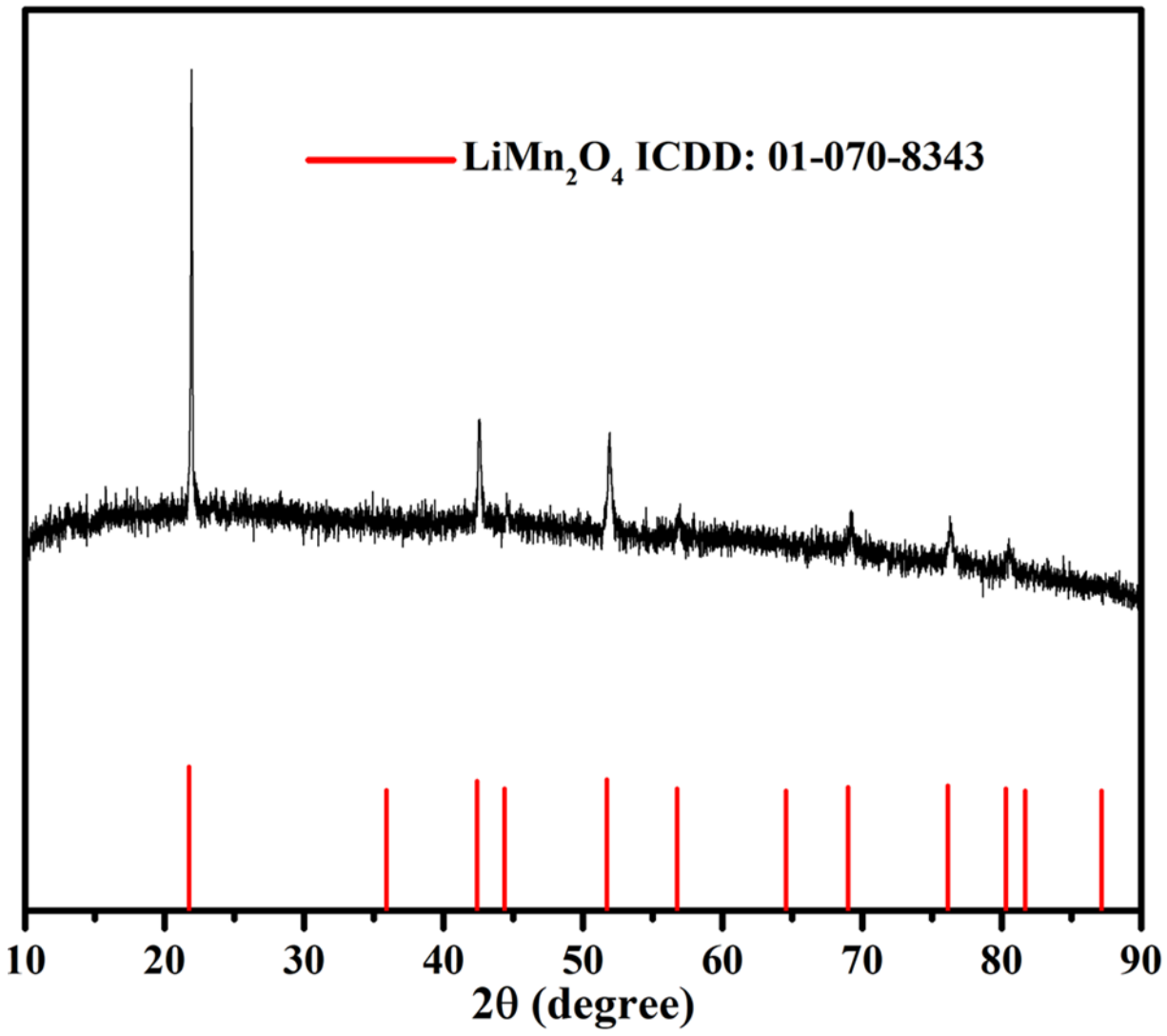

Figure S11. XRD pattern of $LiMn_2O_4$ powder.

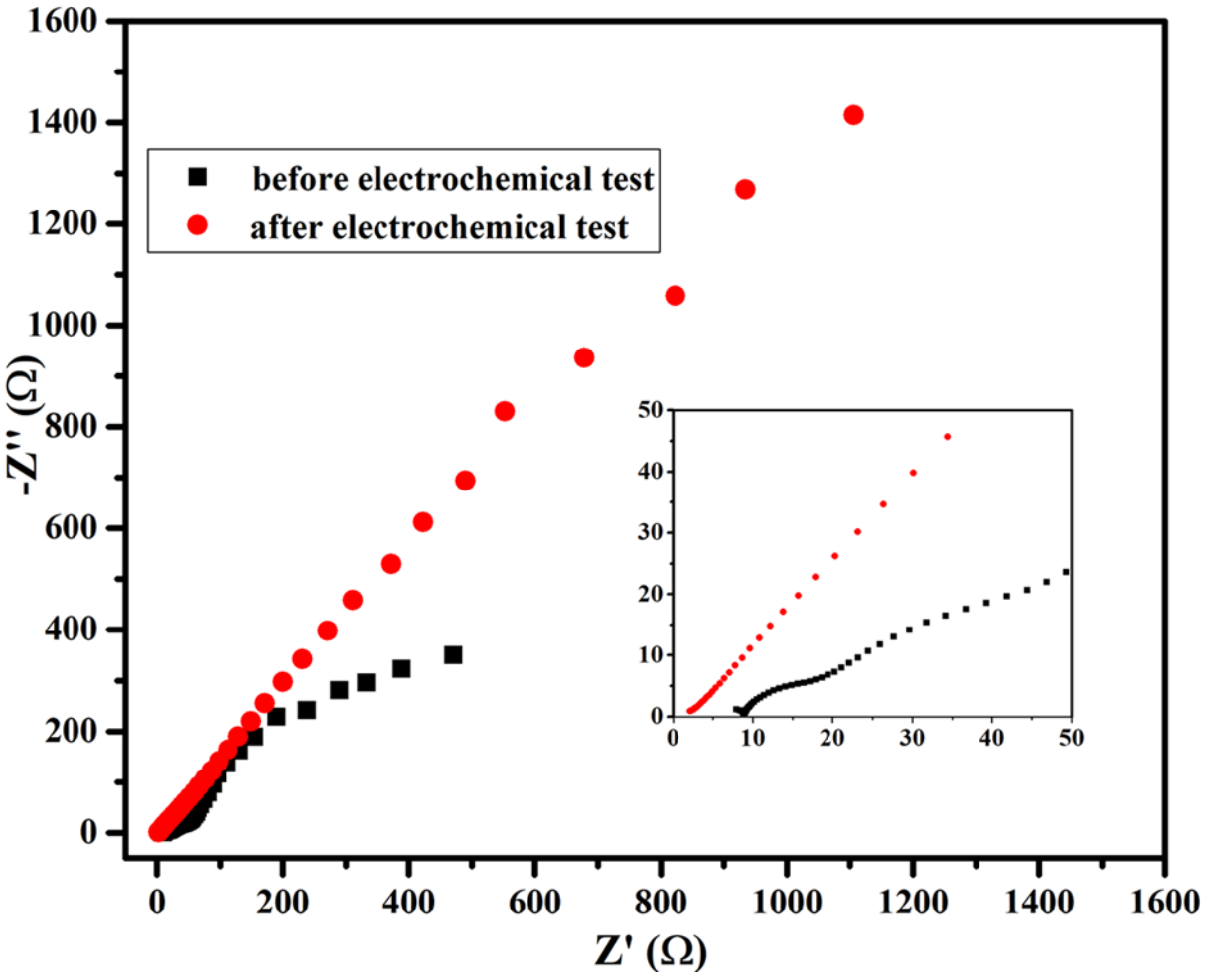

Figure S12. EIS patterns of Zn/$LiMn_2O_4$ coin cell before and after electrochemical cycling test.

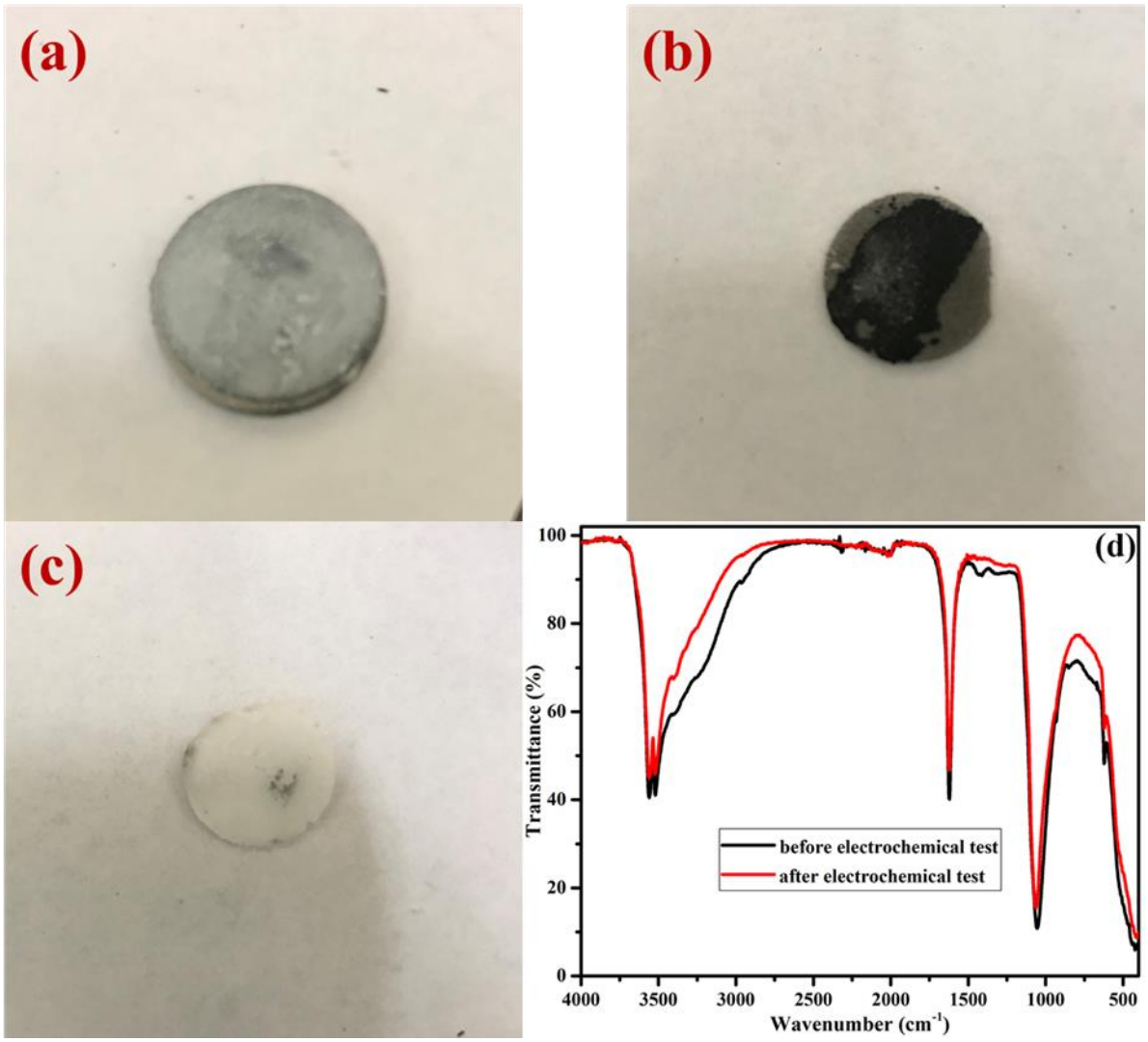

Figure S13. (a-c) Optical images of anode, cathode and electrolyte after electrochemical test. (d) FTIR spectra of the electrolyte before and after electrochemical test.

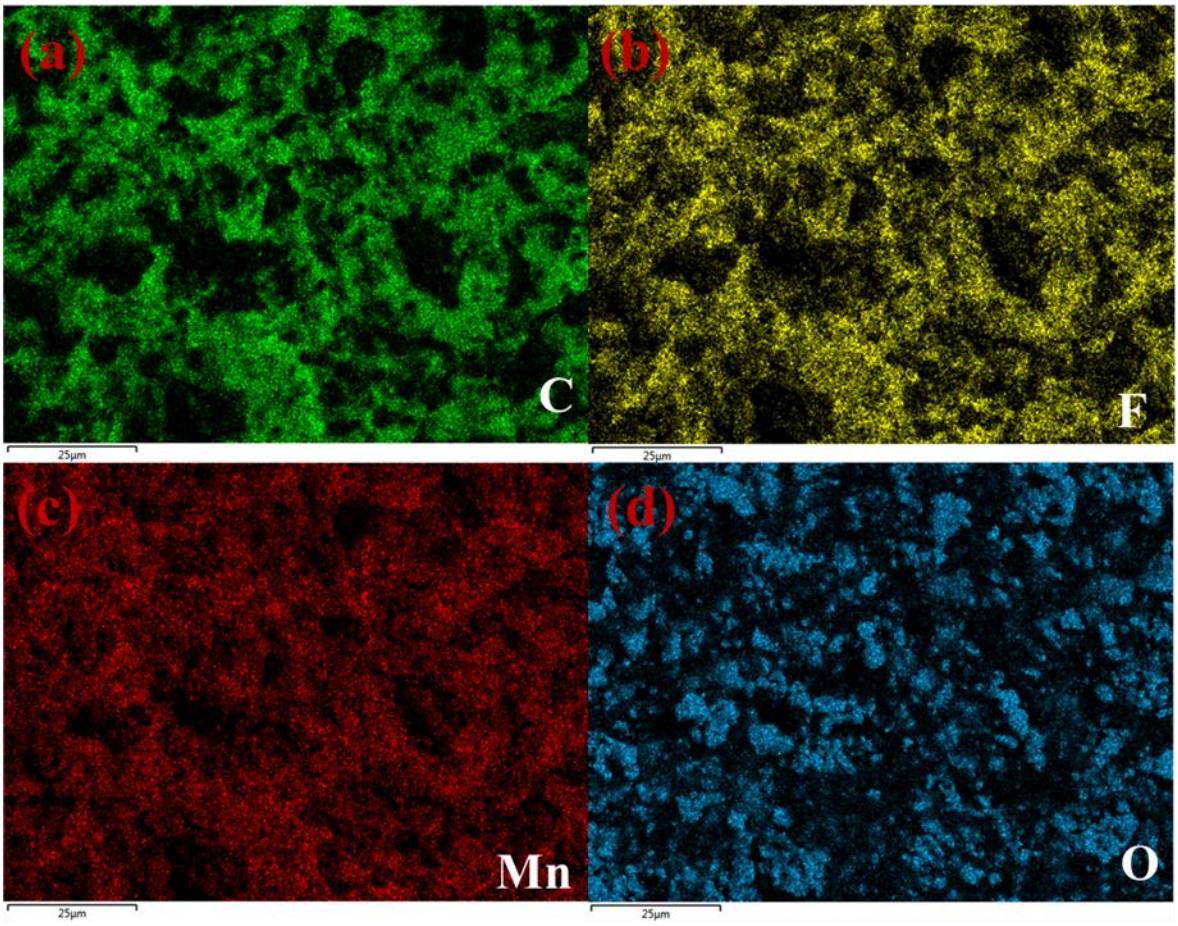

Figure S14. Mappings of C (a), F (b), Mn (c) and O (d) of Ti mesh-$LiMn_2O_4$ electrode before electrochemical test.

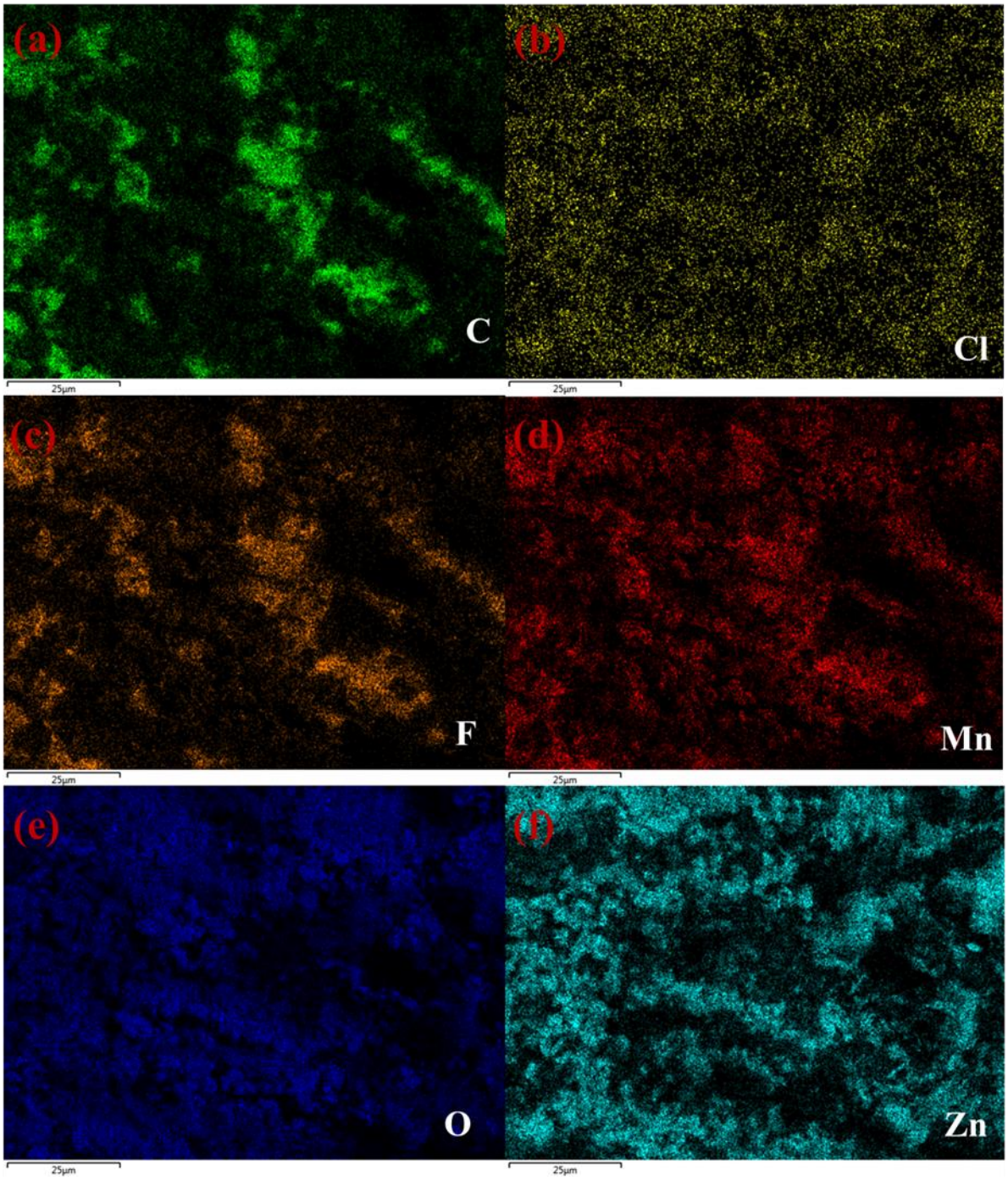

Figure S15. Mappings of C (a), Cl (b), F (c), Mn (d). O (e) and Zn (f) of Ti mesh-$LiMn_2O_4$ electrode after electrochemical test.

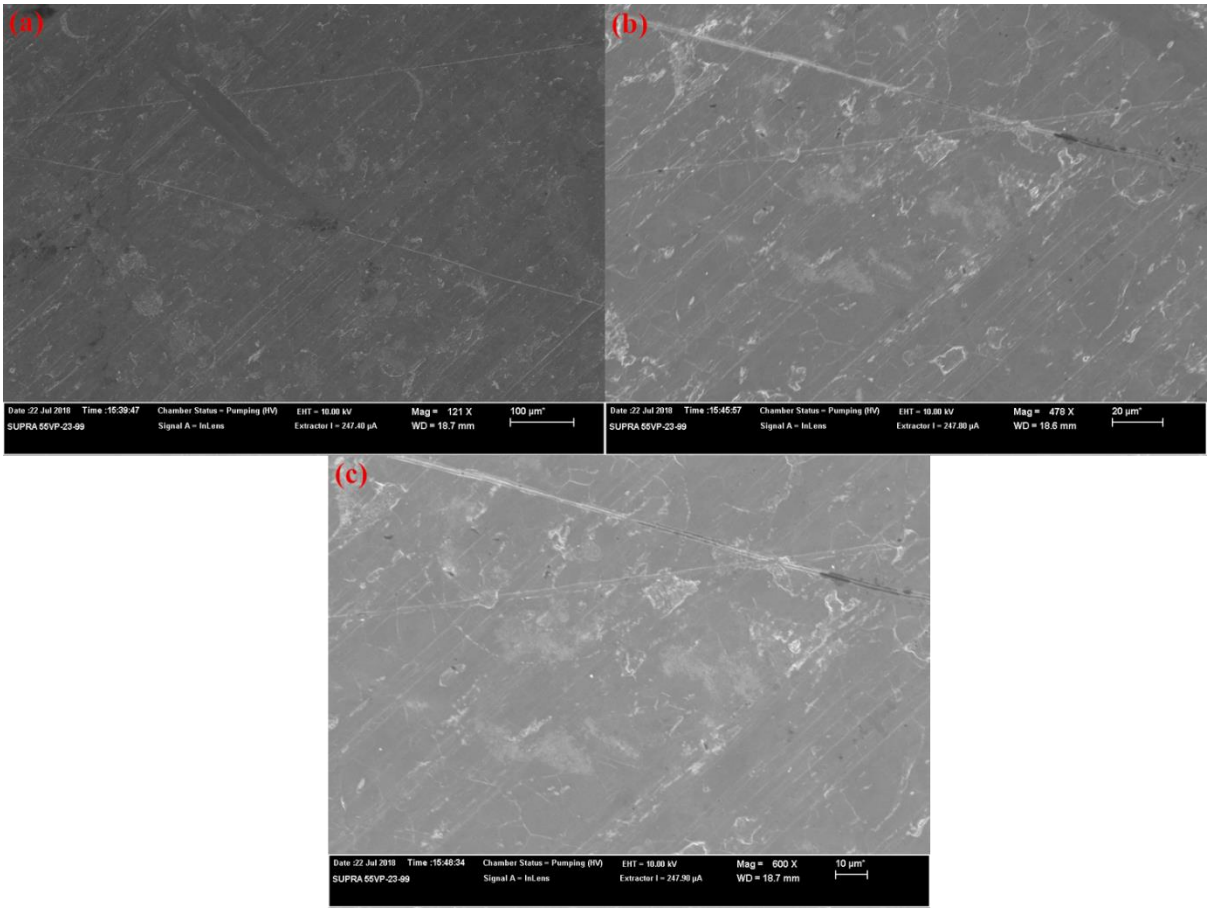

Figure S16. (a, b, c) SEM images of Zn anode after cycling test under different magnifications.

Table of Contents